Chapter 1

Introduction

When Enrico Fermi first theorized back in 1926 the idea for degenerate gas particles that obey Pauli's exclusion principle, he probably did know the effect that his model will have on modern physics in general and ultracold atoms in particular. Since then, The concept of degenerate Fermi gas has helped to unveil new phenomena in various quantum systems and establish itself as a powerful tool in atomic physics. The first realization of an ultracold Fermi gas was only achieved back in 1999 by B. DeMarco and D. Jin [9]. Soon after, numerous groups have tried and succeed in creating similar experiments[19, 15, 39], opening a new era in experimental physics. In those experiments, alkali metals such as ^{6}Li and ^{40}K were originally employed, Due to their energy levels structure and nuclear lifetime stability [45, 13] and until today, they are considered the two main workhorses in the field. The significant advantages of working with these atoms are the simplicity of isolating them from the environment and manipulating their energy state and interaction through light and magnetic fields. An extensive case is the balanced mixture of two spin-state Fermions placed under magnetic potential, and as a consequence, they will undergo a collision process leading to a molecular bound state of two opposite spins pairs. This tool, also known as the Feshbach resonance[22] allows to accesses the strongly interacting regime in a many-body quantum system. The information regarding those fermionic ensemble properties will often be found in their momentum distribution. This intensive quantity can tell whether our gas is in equilibrium, its temperature, and how the Fermi surface looks as we increase interaction and many more physical parameters. For those reasons, measuring the momentum distribution of a trapped cloud is essential to understand quantum gases better. However, most experiments are preform in non-flat traps where the nonuniform density causes energy and length scale dependency in the trap parameters, leading to spatially varying density and eventually prevent the observation of exotic phases such as the FFLO state [12, 36] and maybe other phases as well. To overcome such problems, one needs uniformly flat potential, which is decoupled from any external forces. To do so, one can use blue detuned beams repealing the atoms into a dark "box-like" region in space where the atoms are homogeneously distributed while all other external po-

tentials are canceled. We refer to this light arrangement as a power-law trap with a parameter $p \to \{2, \infty\}$ representing the harmonic and homogeneous limit, respectively. After ensuring the gas is spatially uniform, we can return to measure its momentum distribution. There are a few techniques to measure a momentum-dependent distribution, first by releasing the particles out-of their trapping potential, allowing them to ballistically expend outward from the initial trap location, and taking images at different time-of-flight (ToF) of the expansion. Another option is to use a quarter period expansion [44, 47] this method is based on axial confinement in a perfect harmonic trap and gas expansion inside it. After a quarter period of expansion, the deviation from the center of the cloud is mapped to the axial momentum. Both of those techniques are dependent on releasing the gas from its trap and waiting for it to expand. Nonetheless, we can use Raman spectroscopy instead, having the advantage of measuring the momentum distribution while the ensemble is still trapped. Implementation of the technique requires two laser beams fired simultaneously and transition the atoms at a groundstate to an excited state via a third level coupled to both states. As the cloud absorbed the photons, we see a significant rise in the initially unoccupied excited state as we tune the lasers frequency to be compatible with the two states energy difference. We can translate the two light source frequencies deviation to their relative momentum and, by using energy conservation, also connect this degree of freedom to the ensemble momentum on the Raman beams axis; thus, we relate the converted number of atoms (NoA) to the atomic momentum projection along a single direction. As we will see in the following thesis, the momentum distribution holds information regarding our degenerate Fermi gas of ^{40}K particles with and without interaction involvement.

Outline

The outline of the thesis goes as follows. First, in chapter 2 I will give a theoretical background on our alkali atom and the idea behind the methods we use to capture and probe the gas. This chapter begins with a quick review on ^{40}K and its energy level structure. The following sections will explain some of the possible optical dipole traps and how they are represented mathematically. By adding a new free parameter, I will extend the previous trapping interpretation and deduced several analytical equations for thermodynamical quantities. Since those calculations only hold under flat potential, I will show our dynamical decoupling model to generate a genuinely uniform distribution. Afterward, the discussion would attend to Raman spectroscopy as a method to probe the momentum distribution by transitioning atoms between different atomic states. In this section, a relationship will be develop connecting the Rabi Raman multilevel rate and the light shift to the applied beams intensities and the internal atomic degrees of freedom. Towards the end of the chapter, we will look at the interaction between the spin states and how they affect the gas as we move from weak to strong interaction regimes. In chapter 3, I will illustrate how our main system is built and operates. Next,

I will present the optical box setup design using a DMD and a green laser (532nm). The last section in this chapter will describe the reconstruction and dissection of the Raman system into three subsections. The laser (770nm) and tramped amplifier system, the temperature stable etalon system, and finally the AOM system. The experimental result will appear in chapter 4, where we show how the gas becomes uniform inside the optical box through spin relaxation dynamics. Before we show the gas momentum distribution data, we report the lack of energy levels light shift caused by the Raman beams. Then we present the non-interacting symmetric line-shape produced by the Raman, and by fitting it to the model in chapter 2 we can extract the temperature. The interaction spectral line-shape data is presented in the final section of this chapter, together with a spin imbalanced fitting model. Finally, in chapter 5 there will be a discussion on the strongly interacting Fermions and what can say regarding their spectral line shape data-set. We will explain how we can develop a more accurate model for a spin-balanced mixture on the outlook.

Chapter 2

Theory

This part will clarify the idea behind trapping and probing degenerate Fermi gas and how we can study its physical properties by mapping the ensemble momentum distribution using Raman spectroscopy. First, I will introduce the theory behind the ^{40}K atom, which we use in our system, and then move on to explain the mechanism we employ to trap and manipulate the particles with light and magnetic fields with emphasis on the Raman stimulated transition, and how can we utilize this process to probe the momentum distribution. In the end, this measurement will allow us to extract different parameters related to the gas behavior as we change the interaction between the Fermions in the gas.

2.1 Theory of ultracold Fermi gas of ^{40}K

2.1.1 Energy level structure of ^{40}K

In our lab, we work with ^{40}K, an alkali atom. Having a single valence electron, we can treat it from a QM perspective as electric spin-$\frac{1}{2}$ particle $|\mathbf{S}| = S = \frac{1}{2}$, this electron is creating a magnetic field which then interacts with the nuclei spin $\mathbf{I}$. The electron also has an orbital momentum $\mathbf{L}$, so the electron full angular momentum is described as $\mathbf{J} = \mathbf{L} + \mathbf{S}$ and therefore have eigenvalues $|L - S| \leq J \leq |L + S|$. Suppose the electron is in the orbital ground state. In that case, we can write $\mathbf{L} = 0$, which means that $J = \frac{1}{2}$. For the first excited state, $\mathbf{L} = 1$ and the angular eigenvalues are $J = \frac{1}{2}, \frac{3}{2}$ and looking at the full atom angular momentum $\mathbf{F} = \mathbf{I} + \mathbf{J}$, from this relation, the quantum numbers for the energy levels of the hyperfine structure are $|I - J| \leq F \leq |I + J|$. When an external magnetic field $\mathbf{B}$ is applied to ^{40}K, the hyperfine levels splits in what we call the Zeeman splitting effect. In the case of the lowest manifold $^2\mathrm{S}_{1/2}$ in the lower (higher) hyperfine level $F = \frac{9}{2}\left(\frac{7}{2}\right)$ we have a splitting into $2F + 1$ =10(8) sub-levels. above the ground state manifold, there are two manifold transitioned by the two D-lines, the D1 line $\left(^2\mathrm{S}_{1/2} \rightarrow ^2\mathrm{P}_{1/2}\right)$ and the D2 line $\left(^2\mathrm{S}_{1/2} \rightarrow ^2\mathrm{P}_{3/2}\right)$ as seen in Figure 2.1. We use those D-lines in many applications(optical pumping, MOT, repump, etc.), and we will address mostly the latter as we used it extensively in the

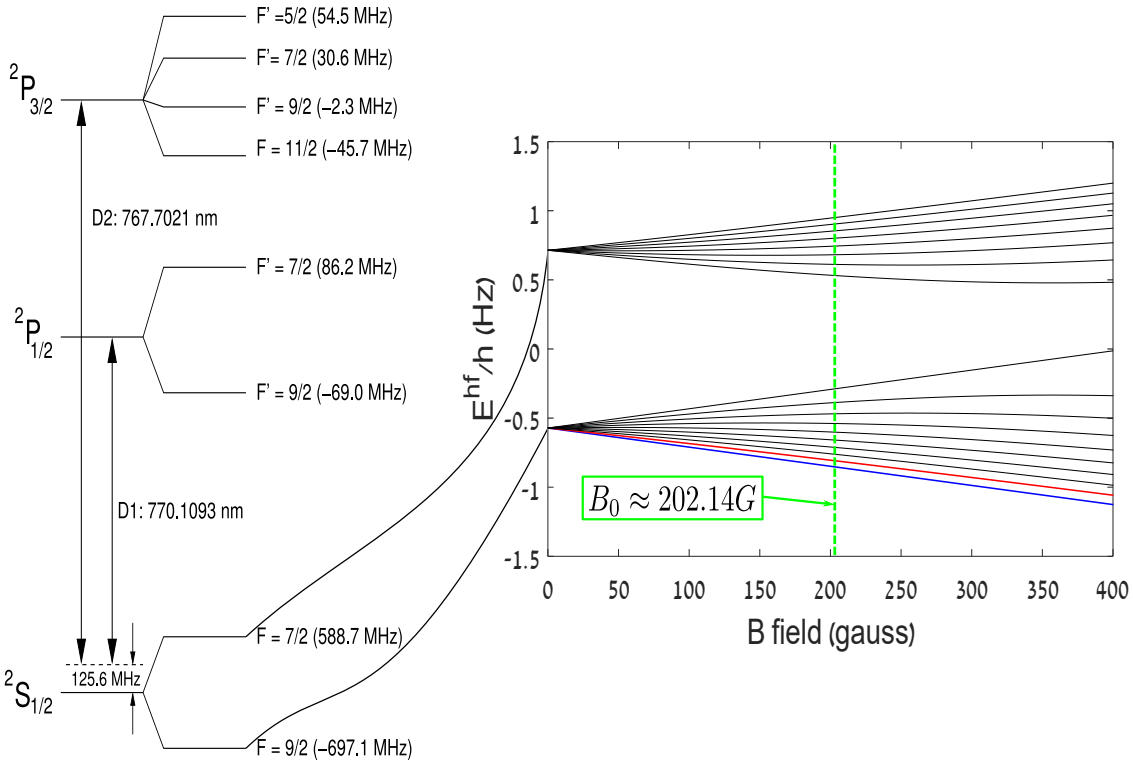

Figure 2.1: Left:the energy level structure of ^{40}K with both the D1 and D2 transition lines.Right:the Zeeman splitting due to external magnetic field of the two lower Hyperfine levels in $^2S_{1/2}$.in green dashed line representing the Feshbach resonance point at the $B_0 = 202.14G$ of the $|\downarrow\rangle = |\frac{9}{2}, -\frac{9}{2}\rangle$ and $|\uparrow\rangle = |\frac{9}{2}, -\frac{7}{2}\rangle$ energy states marked in solid blue and red lines respectively.

Raman spectroscopy experiments at the lab. introducing the hyperfine Hamiltonian with the effect of external magnetic field[45]

$$\hat{H}_{\text{int}} = \hat{H}_{\text{mag}} + \hat{H}_{\text{hf}} \tag{2.1}$$

The first term is due to the external magnetic field

$$\hat{H}_{\text{mag}} = \mu_B \left(g_I \mathbf{I} + g_J \mathbf{J}\right) \cdot \mathbf{B}$$

$\mu_B \approx 1.4$MHz/G is the Bohr magneton. The second term in (2.1) is due to the dipole and quadrupole moments between the electron and the nuclei

$$\hat{H}_{\text{hf}} = a_{\text{hf}} \mathbf{I} \cdot \mathbf{J} + b_{\text{hf}} \frac{6(\mathbf{I} \cdot \mathbf{J})^2 + 3(\mathbf{I} \cdot \mathbf{J}) - 2\mathbf{I}^2\mathbf{J}^2}{2I(2I-1)2J(2J-1)}$$

here the constants a_{hf} , b_{hf} are the hyperfine constant for each magnetic moment. g_I, g_J are the nuclear and electron g-factors. In the ground state of the atom $L = 0 \rightarrow S = J = \frac{1}{2}$ this eliminates the quadrupole term applied together with a low magnetic field the total spin and magnetic field z-component F, m_F becomes good quantum number

and we can correlate them to the *Breit-Rabi formula*[45]

$$E_{\text{int}}(B) = g_I \mu_B m_F B - \frac{a_{\text{hf}}}{4} \pm \frac{a_{\text{hf}}(2I+1)}{4}\sqrt{1 + \frac{4m_F}{2I+1}x + x^2} \tag{2.2}$$

Where $x = \frac{2(g_S - g_I)\mu_B}{a_{\text{hf}}(2I+1)}B$,here Equation 2.2 define the energy level to low magnetic field as seen in Figure 2.1,and it is mostly needed to find the frequency between energy levels under different magnetic fields.The magnetic field not only determines the transition difference it also effects the interaction strength between two spin state in a process known as Feshbach resonance.When dealing with ultracold atoms their internal atomic interaction is dictated by a single parameter which we refer as the scattering length $a(B)$.When for instance two lower Zeeman splitting levels $\{|\uparrow\rangle, |\downarrow\rangle\}$(the blue and red in Figure 2.1) are in the presence of a magnetic field around $202.14G$ [41] they coiled and form a bound molecular state and we preserve this action as due the scattering length is diverging.One final ability of the magnetic field is cooling and trapping the atoms,the procedure involve the use of magneto optical traps (MOT) localizing the particles and using laser cooling decreasing their temperature.However the MOT technique has limitation when it comes to experiments with varying magnetic fields,and therefore a different trapping sequence is needed,for example one that rely on electric dipole interaction with a far detuned light field.

2.2 Optical trap of ultracold atoms

Trapping ultracold atoms is an essential part of the cooling mechanism and without it reaching a degeneracy regime with Fermi gas is impossible. There are two main types of traps when dealing with optical traps. The first is the magneto optical trap as we discussed in the last section and uses the atomic internal magnetic moment to attract them inside the trap. The other is the optical dipole trap which relies on the electric dipole moment and how laser can affect atoms capturing and holding them up to a few seconds. When trying to avoid heating, we use a red-detuned laser far from the atomic resonance. It can be done using a simple Gaussian beam that in its focal point (waist) the atoms are held. This type of trapping is called harmonic trap, and it is used in many cold atoms systems. However, to achieve uniform gas, we need to trap the atoms in a homogeneous trap, also called a box trap. Because the trapping beam is passing in many optical elements, which impose some aberrations and reflection to the light (as seen in Figure 3.3), a perfect optical box potential is impossible to realize. To overcome this problem, we will assume a different type of potential.

2.2.1 Harmonic to homogeneous dipole optical trap

when creating an optical trap we need to consider some monochromatic laser light with frequency ω which we can write as

$$\mathbf{E}(\mathbf{r},t) = \vec{E}(\mathbf{r})e^{i\omega t} \ , \ I(\mathbf{r}) = 2c\epsilon_0 \left|\vec{E}(\mathbf{r})\right|^2 \tag{2.3}$$

assuming an oscillator model together with the semi-classical approach[17], we can write

$$U_{\text{trap}}(\mathbf{r}) = -\frac{3\pi c^2}{2\omega_0^3}\left(\frac{\Gamma}{\omega_0-\omega}+\frac{\Gamma}{\omega_0+\omega}\right) I(\mathbf{r}) \tag{2.4}$$

$$\frac{1}{\tau_{\text{life}}} = \Gamma = \frac{\omega_0^3 \left|\langle i|\mathbf{d}|j\rangle\right|^2}{3\pi\epsilon_0\hbar c^3} \tag{2.5}$$

Here $\Gamma, \omega_0, \epsilon_0, c, \mathbf{d}$ are damping rate (one over lifetime) the on-resonance frequency the vacuum permittivity speed of light and dipole operator respectively. By plugging Equation 2.5 into Equation 2.4 and we assume the rotating wave approximation (RWA) which fulfills $|\omega-\omega_0| = |\Delta| \ll \omega_0$ we can rewrite our equation such that we get

$$U_{\text{trap}}(\mathbf{r}) = \frac{\left|\langle i|\mathbf{d}|j\rangle\right|^2}{\hbar\Delta}\left|\vec{E}(\mathbf{r})\right|^2 \tag{2.6}$$

The $\Delta, \langle i|\,, |j\rangle$ are the one-photon detuning and initial and final state the atoms transitions. Looking at the equation above, we see the essential part it takes in engineering dipole trap, and by taking specific light fields, we can design potentials that correlate to that light intensity and affect the atoms in the desired manner. We note that Equation 2.6 hold as long the detuning is minuscule compere to the resonance frequency. From Equation 2.6 we can categorize optical trap into two types, first red detuned trap ($\Delta < 0$) where the potential is negative, and the trap is attractive, and the potential local minimum is at the maximal intensity region. The second type is blue detuned traps ($\Delta > 0$). The potential is positive repelling atoms toward the potential minimum, which is located at the intensity minimum. The two most common examples are the red detuned harmonic trap and the blue detuned box trap. we can use for harmonic trap a Gaussian beam

$$I_{GB}(r,z) = \frac{2P_0}{\pi w^2(z)} e^{\frac{-2r^2}{w^2(z)}} \ , \ w(z) = w_0\sqrt{1+\left(\frac{z}{z_R}\right)^2} \tag{2.7}$$

Where we define w_0, P_0, z_R as the waist minimum of the beam, the power amplitude of the beam, and the Rayleigh range, which can be written as $z_R = \pi w_0^2/\lambda$ and λ is the light wavelength. Again Equation 2.6 can relate the potential to the intensity and by approximating around zero to get

$$U_{GB}(r,z) \approx U_0\left[\left(\frac{r}{\sqrt{2}w_0}\right)^2+\left(\frac{z}{z_R}\right)^2\right] \tag{2.8}$$

This type of trap potential is heavily dependent on spatial parameters,the radial and vertical frequencies $\omega_r = \sqrt{4U_0/mw_0^2}$ and $\omega_z = \sqrt{2U_0/mz_R^2}$. These trap frequencies defines the length scale of the trap and due to its spatial varying nature the held density is predominately reside in the center and we can observe a phase separation over the atomic cloud. To overcome this issue, we can construct a flat-box potential defined as

$$U(\mathbf{r}) = \begin{cases} 0 & \|\mathbf{r}\| < r_0 \\ U_0 & o.w. \end{cases} \tag{2.9}$$

Here $\|\mathbf{r}\| = \sqrt{x^2+y^2+z^2}$ is the trap effective radius. In this potential, the cloud is independent of any energy or length scale of the trap. generating such potential is practically impossible due to light diffraction and imperfection of optical elements, so instead, we can approximate to a power-law potential which in general writes

$$U(\mathbf{r}) = U_0 \left(\frac{\|\mathbf{r}\|}{r_0}\right)^p \tag{2.10}$$

If we take the limits $p \to \{2, \infty\}$ we will get back the harmonic and homogeneous potentials ,respectively. Because those two boundaries are well established in the literature [24, 5], we can easily verify our results in a more realistic power-law potential, and we will now examine this idea further.

2.2.2 Power-law trap in Fermi gas

If we want to understand how optically trapping atoms affect the ensemble distribution, we need to account for the particles statistic so when dealing with Fermions, we assume a momentum and spatially density according to the Fermi-Dirac distribution.

$$n(\mathbf{k},\mathbf{r}) = \frac{1}{e^{(\mathcal{H}(\mathbf{k},\mathbf{r})-\mu)/k_BT}+1} = \frac{1}{\eta^{-1}e^{\left(\frac{(\hbar\mathbf{k})^2}{2m}+U(\mathbf{r})\right)/k_BT}+1} \tag{2.11}$$

Here $\eta = e^{\mu/k_BT}$ is the fugacity, and m, μ and T are the mass of the particles, the chemical potential, and temperature. We can assume some trapping potential that is capturing our atomic ensemble.

$$U(\mathbf{r}) = \left(U_x^{\frac{2}{p}}\left(\frac{x}{x_0}\right)^2 + U_y^{\frac{2}{p}}\left(\frac{y}{y_0}\right)^2 + U_z^{\frac{2}{p}}\left(\frac{z}{z_0}\right)^2\right)^{\frac{p}{2}} \tag{2.12}$$

This type of power-law potential is a generalization of optical trap potentials, and in the case where $U_z = U_y = U_x = U_0$ and $p = 2$ we get and harmonic trap, and when $p \to \infty$ we get a perfect box trap. Those two limits are known, and we would like to obtain a model between those limits as a function of the power-law parameter p. So

first, let us look at momentum distribution for

$$n(\mathbf{k}) = \iiint n(\mathbf{r},\mathbf{k}) = \frac{1}{(2\pi)^3}\iiint \frac{dxdydz}{\eta^{-1}e^{\left\{\frac{\hbar^2\mathbf{k}^2}{2m}+U(\mathbf{r})\right\}\Big/k_BT}+1} =$$

$$\frac{1}{(2\pi)^3}\iiint \frac{dxdydz}{\eta^{-1}e^{\left\{\frac{\hbar^2\mathbf{k}^2}{2m}+\left(U_x^{\frac{2}{p}}\left(\frac{x}{x_0}\right)^2+U_y^{\frac{2}{p}}\left(\frac{y}{y_0}\right)^2+U_z^{\frac{2}{p}}\left(\frac{z}{z_0}\right)^2\right)^{\frac{p}{2}}\right\}\Big/k_BT}+1} =$$

$$\frac{x_0y_0z_0}{8\pi^3\left(U_xU_yU_z\right)^{\frac{1}{p}}}\iiint \frac{dXdYdZ}{\eta^{-1}e^{\left\{\frac{\hbar^2\mathbf{k}^2}{2m}+\left(X^2+Y^2+Z^2\right)^{\frac{p}{2}}\right\}\Big/k_BT}+1} =$$

$$\frac{x_0y_0z_0}{2\pi^2\bar{U}^{3/p}}\int_0^\infty \frac{R^2dR}{\eta^{-1}e^{\left\{\frac{\hbar^2\mathbf{k}^2}{2m}+R^p\right\}\Big/k_BT}+1} = -\frac{V_0\Gamma\left(\frac{3}{p}+1\right)}{6\pi^2}\mathrm{Li}_{\frac{3}{p}}\left(-\eta e^{-\frac{(\hbar\mathbf{k})^2}{2mk_BT}}\right)\left(\frac{k_BT}{\bar{U}}\right)^{\frac{3}{p}}$$

where we define

$$\begin{cases} X = x/U_x^{-\frac{1}{p}}x_0\ ,\ dX = dx/U_x^{-\frac{1}{p}}x_0 \\ Y = y/U_z^{-\frac{1}{p}}y_0\ ,\ dY = dy/U_x^{-\frac{1}{p}}y_0 \\ Z = z/U_z^{-\frac{1}{2}}z_0\ ,\ dZ = dz/U_x^{-\frac{1}{p}}z_0 \end{cases}\ ,\ \begin{cases} R^2 = X^2+Y^2+Z^2 \\ dXdYdZ = 4\pi R^2dRd \end{cases}$$

if we integrate over momentum we get the spatial density

$$n(\mathbf{r}) = \frac{1}{(2\pi)^3}\iiint \frac{d^3\mathbf{k}}{\eta^{-1}e^{\left(\frac{\hbar^2\mathbf{k}^2}{2m}+V(\mathbf{r})\right)\Big/k_BT}+1} = \tag{2.13}$$

$$\int \frac{(\sqrt{2}\pi)^{-2}k^2dk}{\eta^{-1}e^{\beta V(\mathbf{r})}e^{\left(\beta\frac{\hbar^2}{2m}k^2\right)}+1} = -\frac{\mathrm{Li}_{\frac{3}{2}}\left(-\eta e^{-\beta U(\mathbf{r})}\right)}{\lambda_{dB}^3}$$

here we define $\beta \equiv \frac{1}{k_BT}$ and $\lambda_{dB} = \sqrt{\frac{2\pi\hbar^2}{mk_BT}}$ the de-Broglie wavelength. The next step is to use the Fermi Normalized units in the momentum integral and use the normalization condition in $T = 0$. so we can write with the use of Equation A.1

$$N = \frac{\iiint n(\mathbf{k})\,d^3\mathbf{k}}{(2\pi)^3} = -\int \frac{V_0}{(2\pi)^3}\Gamma\left(\frac{3}{p}+1\right)\mathrm{Li}_{\frac{3}{p}}\left(-\frac{e^{-\frac{(\hbar k)^2}{2mk_BT}}}{\eta}\right)\left(\frac{k_BT}{\overline{U}}\right)^{\frac{3}{p}}k^2dk \tag{2.14}$$

$$\begin{cases} T/T_F \to t_F \\ k \to K = k/k_F \end{cases} \Rightarrow -\int \frac{V_0k_F^3}{(2\pi)^3}\Gamma\left(\frac{3}{p}+1\right)\mathrm{Li}_{\frac{3}{p}}\left(-\frac{e^{-\frac{K^2}{t_F}}}{\eta}\right)\left(\frac{t_F}{\overline{U}/E_F}\right)^{\frac{3}{p}}K^2dK =$$

$$\frac{V_0k_F^3}{8\pi^{3/2}}\Gamma\left(\frac{3}{p}+1\right)\mathrm{Li}_{\frac{3}{p}+\frac{3}{2}}(-\eta)\left(\frac{t_F}{\overline{U}/E_F}\right)^{\frac{3}{p}}t_F^{\frac{3}{2}}$$

We are left with finding k_F and invert the relation to find η. From the limit $T \to 0$, we get that the momentum distribution is a Heaviside function both in momentum and in

space and $\mu = E_F$. After we fix our total density for general T, we can then find the fugacity. so we integrate on both momentum and space in 3D, which gives

$$N_{T=0} = \frac{1}{(2\pi)^3}\iiint n\left(\mathbf{r},\mathbf{k}\right)d^3\mathbf{k}d^3\mathbf{r} = \frac{1}{(2\pi)^3}\iiint \theta\left(E_F - \frac{\hbar^2\mathbf{k}^2}{2m} - U\left(\mathbf{r}\right)\right)d^3\mathbf{k}d^3\mathbf{r} =$$
$$\frac{1}{(2\pi)^3}\iiint \frac{x_0y_0z_0}{\left(U_xU_yU_z\right)^{1/p}}\int_0^\infty \theta\left(E_F - \frac{\hbar^2\mathbf{k}^2}{2m} - R^p\right)R^2dRd^3\mathbf{k} =$$
$$\frac{V_0}{\left(2\pi\bar{U}^{1/p}\right)^3}\iiint \theta\left(E_F - \frac{\hbar^2\mathbf{k}^2}{2m}\right)\left(E_F - \frac{\hbar^2k^2}{2m}\right)^{3/p}d^3\mathbf{k} =$$
$$\frac{4\pi V_0}{(2\pi)^3}\left(\frac{E_F}{\bar{U}}\right)^{\frac{3}{p}}\int_0^{k_F}\left(1-\frac{\hbar^2k^2}{2mE_F}\right)^{\frac{3}{p}}k^2dk = \frac{V_0k_F^3}{8\pi^{\frac{3}{2}}}\left(\frac{E_F}{\bar{U}}\right)^{\frac{3}{p}}\frac{\Gamma\left(\frac{3}{p}+1\right)}{\Gamma\left(\frac{5}{2}+\frac{3}{p}\right)}$$

from this relation we can invert to find the solution for $k_F = \frac{\sqrt{2mE_F}}{\hbar}$ for any power law as function of density $n_0 = n\left(T=0\right) = N_{T=0}/V_0$. So after some algebra we get

$$k_F = \left(\frac{2m\bar{U}}{\hbar^2}\right)^{\frac{1}{2+p}}\left(\frac{8\pi^{\frac{3}{2}}\Gamma\left(\frac{5}{2}+\frac{3}{p}\right)}{\Gamma\left(\frac{3}{p}+1\right)}n_0\right)^{\frac{p}{(6+3p)}} \tag{2.15}$$

we check in both homogeneous and harmonic limits and see that indeed this equation holds for example when $p \to \infty$ we get a perfect box and then $k_F = \left(6\pi^2 n\right)^{\frac{1}{3}}, n = \frac{N}{V_0}$.plugging this back to the Equation 2.14 we see that

$$\frac{k_F^3}{8\pi^{\frac{3}{2}}}\Gamma\left(\frac{3}{p}+1\right)\mathrm{Li}_{\frac{3}{p}+\frac{3}{2}}\left(-\eta\right)\left(\frac{E_F}{\bar{U}}\right)^{\frac{3}{p}}t_F^{\frac{3}{p}+\frac{3}{2}} = n_0 = \frac{k_F^3}{8\pi^{\frac{3}{2}}}\left(\frac{E_F}{\bar{U}}\right)^{\frac{3}{p}}\frac{\Gamma\left(\frac{3}{p}+1\right)}{\Gamma\left(\frac{5}{2}+\frac{3}{p}\right)} \tag{2.16}$$

after elimination from both sides and inverting the polylogarithm function

$$\eta_p(t_F) = -\mathrm{Li}^{-1}_{\frac{3}{p}+\frac{3}{2}}\left(\frac{t_F^{-\left(\frac{3}{2}+\frac{3}{p}\right)}}{\Gamma\left(\frac{5}{2}+\frac{3}{p}\right)}\right) \tag{2.17}$$

We can now write the full 3D momentum distribution in terms of the Fermi natural units

$$n_{3D}(K) = -\frac{4t_F^{\frac{3}{p}}\Gamma\left[\frac{5}{2}+\frac{3}{p}\right]\mathrm{Li}_{\frac{3}{p}}\left(-\eta_p(t_F)e^{-\frac{K^2}{t_F}}\right)}{3\sqrt{\pi}}$$

by integrating twice we can also write the 1D momentum distribution and plot it accordingly

$$n_{1D}(k_x) = \iint n_{3D}(K)dk_ydk_z = -\frac{4\sqrt{\pi}t_F^{\frac{3+p}{p}}\Gamma\left[\frac{5}{2}+\frac{3}{p}\right]\mathrm{Li}_{\frac{3+p}{p}}\left(-\eta_p(t_F)e^{-\frac{(k_x/k_F)^2}{t_F}}\right)}{3} \tag{2.18}$$

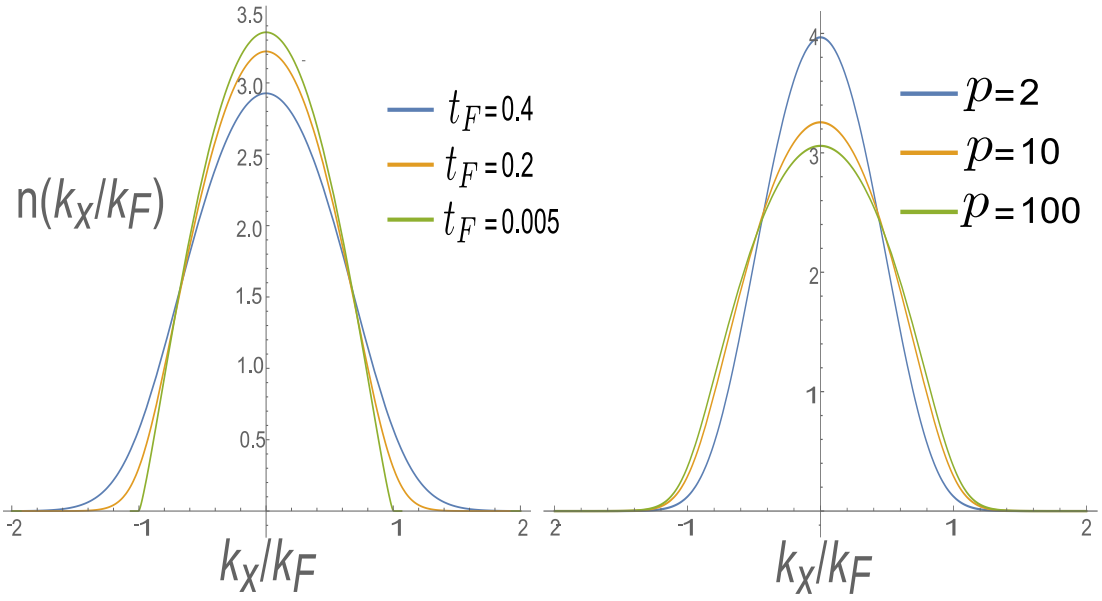

Figure 2.2: plotting equation Equation 2.18 on the left side we see the effect of changing $t_F = \frac{T}{T_F}$ when reaching to lower temperatures ($t_F < 0.005$) the plot did converge appropriate.On the right, we plot the effect of changing the power-law parameter, when $p = 2$ represents harmonic trap, and $p = 100$ is an almost homogeneous trap.

The entire derivation is consistent with the $p = 2$ and $p \to \infty$ limits for all calculated quantities and functions, thus validating our results. We can look at different powers and temperature scales and plot the 1D momentum distribution and see the deviation from the homogeneous and harmonic limits as seen in Figure 2.2. Even though the power-law trap is only an approximation of a homogeneous trap, we would still want to ensure a uniform gas distribution in this type of potential, but this is not always the case when working with two spin-state Fermionic systems.

2.2.3 Dynamical Decoupling scheme to generate a uniform gas

Creating a uniform gas inside a power-law trap means that the full single-particle potential the atoms experience is flat. So throughout the experiments in the trap, we most mitigate any external forces other than the optical potential holding the atoms. Gravity becomes an apparent problem when dealing with a degenerate gas system, and The particles are predominately occupying one region and not distributed equally. We can counteract gravity using an equal amplitude magnetic gradient force applied on the same axis in the opposite direction. However, When dealing with a mixture of two spin-state having different magnetic moments, adding a magnetic field will cause each spin to experience an unequal force and prevent the potential to genuinely be flat as seen in LSH in Figure 2.3. Nevertheless, we can decouple the spins from gravity by employing an rf pulse, inducing a rapid spin rotation. This dynamical decoupling (DD) driving pulse causes the atoms in both spins to feel the same time average flat potential, leading

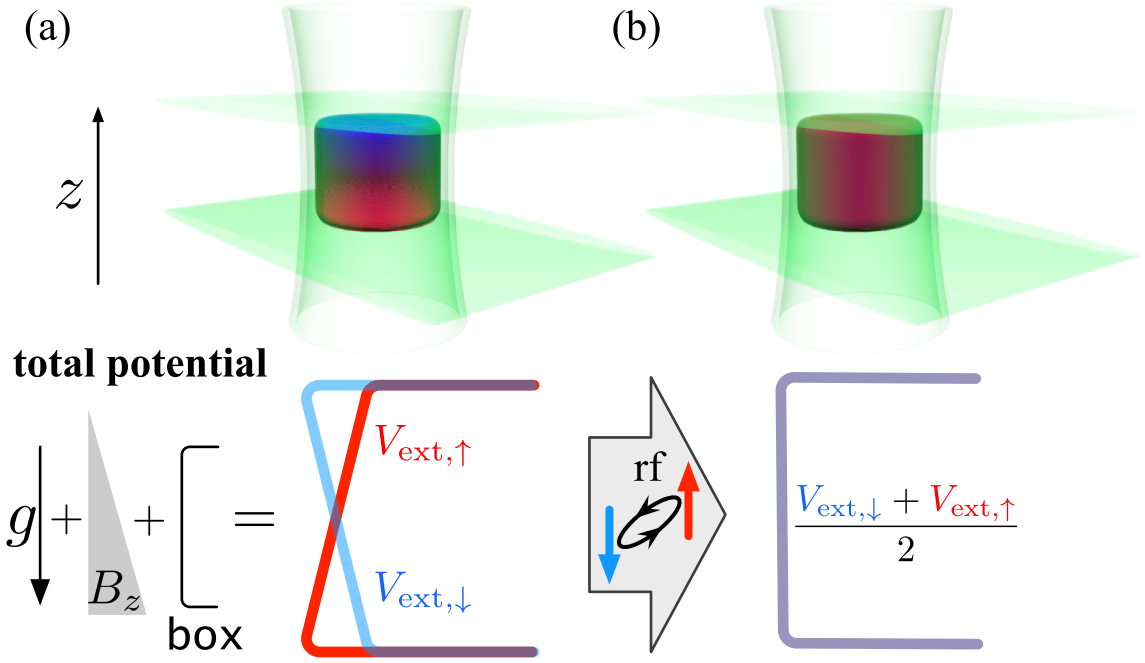

Figure 2.3: **(a)** A 3D image of the gas is held in an optical box potential while experiencing gravitational and magnetic potentials inside the trap. The gas is composed of two spin states, the $|\uparrow\rangle$ and $|\downarrow\rangle$ (shown in red and blue, respectively), occupying the lower and upper regions in the trap due to their different magnetic moment.**(b)** The gas ensemble after applying and a resonant rf field that periodically drives a rapid spin rotation, thus creating an effective spin-independent average potential given by Equation 2.23, leading to a uniform atomic gas. Importantly we do not affect the many-body behavior by this dynamical decoupling pulse.

to a homogeneous atomic cloud as seen on RHS in Figure 2.3. We want to show that we can implement this sequence without heating the gas, so firstly, we will theoretically prove the Hamiltonian is unaffected in this section, and on chapter 4 we will show it experimentally. Let us start by writing the full Hamiltonian with three contribution $\hat{H} = \hat{H}_0 + \hat{H}_{\text{int}} + \hat{H}_{\text{rf}}$ if consider a two fermionic states $s \in \{|\uparrow\rangle, |\downarrow\rangle\}$ together with their second quantization fermionic field operators which obey the anti-commutation relation $\left\{\hat{\Psi}_s(\mathbf{r}), \hat{\Psi}^\dagger_{s'}(\mathbf{r}')\right\} = \delta^{s'}_s \delta(\mathbf{r} - \mathbf{r}')$ here $\delta^{s'}_s$ and $\delta(\mathbf{r} - \mathbf{r}')$ are the Kronecker and Dirac delta, respectively.We then can write each part separably as follow

$$\hat{H}_0 = \sum_{s=\{\uparrow,\downarrow\}} \int d\mathbf{r} \hat{\Psi}^\dagger_s(\mathbf{r}) \left(-\frac{\hbar^2 \nabla^2}{2m} + V_{\text{ext},s}(\mathbf{r}) \right) \hat{\Psi}_s(\mathbf{r}) \tag{2.19}$$

$$\hat{H}_{\text{int}} = \iint d\mathbf{r} d\mathbf{r}' V(\mathbf{r}, \mathbf{r}') \Psi^\dagger_\uparrow(\mathbf{r}) \Psi^\dagger_\downarrow(\mathbf{r}') \Psi_\downarrow(\mathbf{r}') \Psi_\uparrow(\mathbf{r}) \ , \ V(\mathbf{r}, \mathbf{r}') = g\delta(\mathbf{r} - \mathbf{r}') \frac{\partial}{\partial r} r \tag{2.20}$$

$$\hat{H}_{\text{rf}} = \frac{\hbar}{2} \int d\mathbf{r} \ \Omega e^{i\omega_0 t} \left(e^{i\omega_{\text{rf}} t} + e^{-i\omega_{\text{rf}} t} \right) \hat{\Psi}^\dagger_\uparrow(\mathbf{r}) \hat{\Psi}_\downarrow(\mathbf{r}) + h.c. \tag{2.21}$$

The first part account for the single-particle energy where the potential energy is given by $V_{\text{ext},s} = V_{\text{trap}} + (mg + \mu_s B_z)\, z$, where the first term is optical flat potential, the second and third accounts for the gravitational and magnetic potentials which we desire to cancel each other. The two body interaction potential $V(\mathbf{r}, \mathbf{r}')$ represent the short range contact interaction where $g = \frac{4\pi\hbar^2}{m} a(B)$.Here $m, a(B)$ is the particle mass and the scattering length which enable to tune the interaction by changing the field thus transitioning from the BEC side to BCS.Finally the rf part where Ω is the Rabi frequency and $\omega_{\text{rf}} = \omega_0$ are the rf and bare frequency which we set to be equal and also $\omega_0 \gg \Omega$ in our experiment.This means we can use the rotating wave approximation (RWA) and consider $\hat{H}_{\text{rf}} = \frac{\hbar}{2} \int d\mathbf{r} \Omega \hat{\Psi}^\dagger_\uparrow(\mathbf{r}) \hat{\Psi}_\downarrow(\mathbf{r}) + h.c.$ To see the effect of the rf field, we perform a unitary transformation $\hat{U} = e^{\frac{i}{\hbar}\hat{H}_{\text{rf}}}$ eliminating this term in the Hamiltonian while moving to a reference frame of the rotating spins. under this transformation, the Fermionic field become

$$\begin{aligned} \hat{U}\hat{\Psi}^\dagger_\uparrow(\mathbf{r})\hat{U}^\dagger &= \cos\left(\frac{\Omega t}{2}\right)\hat{\Psi}^\dagger_\uparrow(\mathbf{r}) + i\frac{\Omega^*}{|\Omega|}\sin\left(\frac{\Omega t}{2}\right)\hat{\Psi}^\dagger_\downarrow(\mathbf{r}) \\ \hat{U}\hat{\Psi}^\dagger_\downarrow(\mathbf{r})\hat{U}^\dagger &= i\frac{\Omega}{|\Omega|}\sin\left(\frac{\Omega t}{2}\right)\hat{\Psi}^\dagger_\uparrow(\mathbf{r}) + \cos\left(\frac{\Omega t}{2}\right)\hat{\Psi}^\dagger_\downarrow(\mathbf{r}) \quad . \end{aligned} \tag{2.22}$$

It is proven in the (appendix A) that first ,indeed the fields transform as follow and second that $\hat{H}_{\text{int}} \xrightarrow{\hat{U}} \hat{H}_{\text{int}}$ is invariant under this action if the potential is symmetric $V(\mathbf{r}', \mathbf{r}) = V(\mathbf{r}, \mathbf{r}')$. On the other hand, if we examine $\hat{H}_0$, the only apparent difference is at the external potential, which becomes time-dependent in both the off and on diagonal terms, as seen in (appendix A). By time-averaging, the off diagonal vanishes while the diagonal terms become spin independent,

$$\langle \hat{U}\hat{H}_{\text{ext}}\hat{U}^\dagger \rangle_\tau = \sum_{\{s=\uparrow,\downarrow\}} \int d\mathbf{r} \hat{\Psi}^\dagger_s(\mathbf{r}) \frac{V_{\text{ext},\uparrow}(\mathbf{r}) + V_{\text{ext},\downarrow}(\mathbf{r})}{2} \hat{\Psi}_s(\mathbf{r}) \tag{2.23}$$

where $\hat{H}_{\text{ext}}$ and $\langle\cdot\rangle_\tau$ denote the contribution of the external potential to $\hat{H}_0$ and the time average over a long duration $\tau \gg 2\pi/\Omega$, respectively.therefore obtain that, to first order in the Magnus expansion [4], the rf driving generates an effective Hamiltonian with a spin-independent external potential and all other terms the same as in the non-driven Hamiltonian. Hence, we expect to get the same many-body behavior as a stationary system in the spin-averaged external potential. In our experiment, we set the magnetic field in the axial direction $B_z = -\frac{2mg}{\mu_\downarrow + \mu_\uparrow}$ and we see that if $\mu_\downarrow \neq \mu_\uparrow$ the external potential will not be truly flat. However,by expressing it in the form of Equation 2.23 our requirement to achieve uniformity through cancellation of gravity is met,and we can now proceed to study the gas with the Raman spectroscopy tool.

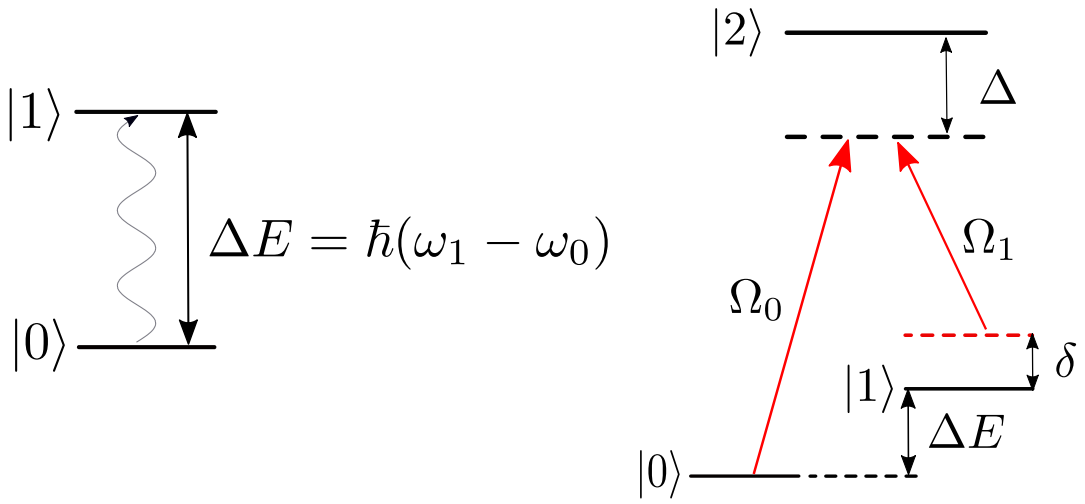

Figure 2.4: (a) a two level system with the energy different of the ΔE and to excite the atom a photon with the frequency difference is required,(b) three level system where we have a third level $|2\rangle$. the transition is made to a virtual level that is detuned by Δ.Two laser beams are coupled between each ground level to the excited third level with the appropriate Rabi frequency

2.3 Stimulated Raman transition

After the cloud became homogeneous we would like to explore its momentum distribution using the Raman beams.Before we dive into the full Raman transition scheme we should start with a model of two level system that can be described by $|0\rangle, |1\rangle$.first we can drive the system to transfer an atom from one level to another by using light we can refer to this process as a single photon transition a one photon transition between those two levels. Adding a third level $|2\rangle$ changes the process so we can transfer atoms using that level. In this schema, there are two lasers involved to drive the atomic transition. we can see those two processes in the Figure 2.4 in a three level system where $|\Psi\rangle = \{|0\rangle, |1\rangle, |2\rangle\}$ is our basis we can with the rotating wave approximation and setting the lowest ground state energy to zero we get

$$\hat{H}_R = \frac{\hbar}{2}\begin{pmatrix} 0 & 0 & \Omega_0 \\ 0 & -2\delta & \Omega_1 \\ \Omega_0^* & \Omega_1^* & -2\Delta \end{pmatrix} \tag{2.24}$$

we denote Δ, δ as the one photon detuning and two photon detuning and Ω_i are the Rabi frequencies.connected to the atomic structure and the light field by this relationship

$$\Omega_i = \frac{\langle i| \boldsymbol{d} \cdot \mathbf{E}(\mathbf{r}, t) |2\rangle}{\hbar} \tag{2.25}$$

$\boldsymbol{d} = q\boldsymbol{r}$ is the transition dipole moment and $\mathbf{E}$ is laser light field. i, j represents the energy levels the atoms transitioning from and to. using the time-dependent Schrödinger

equation in this system and assuming that $\Delta \gg \Omega_i$ we can treat the $|2\rangle$ as an empty state effectively and therefore, an effective two level Hamiltonian

$$\hat{H}_R^{\text{eff}} = \frac{\hbar}{2}\begin{pmatrix} \frac{|\Omega_1(\mathbf{r})|^2}{2\Delta} + 2\delta & \frac{\Omega_1(\mathbf{r})\Omega_0^*(\mathbf{r})}{2\Delta} \\ \frac{\Omega_0(\mathbf{r})\Omega_1^*(\mathbf{r})}{2\Delta} & \frac{|\Omega_0(\mathbf{r})|^2}{2\Delta} - 2\delta \end{pmatrix}$$

we refer to the off diagonal elements as the transition frequency also known as the Rabi frequency

$$\Omega_R = \frac{\Omega_1\Omega_0^*}{2\Delta} \tag{2.26}$$

by looking at the diagonal elements we can define another quantity the AC-stark light shift

$$\delta_{AC} = \frac{|\Omega_1(\boldsymbol{r})|^2}{4\Delta} - \frac{|\Omega_0(\boldsymbol{r})|^2}{4\Delta} \tag{2.27}$$

this then also shift the two photon detuning giving an effective detuning

$$\delta_{\text{eff}} = \delta - \delta_{AC} \tag{2.28}$$

duo to this effective detuning the frequency of transition needs to be modify

$$\tilde{\Omega}_R = \sqrt{\Omega_R^2 + \delta_{\text{eff}}^2} \tag{2.29}$$

this is the generalized Rabi frequency.

2.3.1 Raman transition in ^{40}K

As seen in the previous section inducing Raman transition is a three level procedure, but there are many energy levels in ^{40}K.To calculate the Rabi frequency and light shift accurately, we need a more complex schema similar to [2]. By taking into account selection rules and considering the effect of cross-coupling due to both lasers' effects, we can elevate our model to fit the multiple level transition, which is the realistic description of our system. We start by donating our counter-propagating Raman beams, as E_P, E_S for the pump and stocks laser. The sampling using the Raman is through $|\frac{9}{2}, -\frac{7}{2}\rangle \leftrightarrow |\frac{9}{2}, -\frac{5}{2}\rangle$ levels providing an insight on the interacting between $|\frac{9}{2}, -\frac{9}{2}\rangle \leftrightarrow |\frac{9}{2}, -\frac{7}{2}\rangle$ levels as the Feshbach resonance is found between those two state in our set magnetic field thus probing their strongly correlated behavior.

2.3.2 Light polarization and Geometric factor

If we look at Equation 2.25 we can see two main elements first is the dipole of the atom, and the second is the field. let us start with the latter. We can write

$$\vec{E}_{\mathcal{L},q}(\mathbf{r}) = E_{\mathcal{L}}(z)\hat{e}_q = \Re\left[E_{\mathcal{L}}e^{i(\omega_q t - k_q z)}\hat{e}_q)\right] \tag{2.30}$$

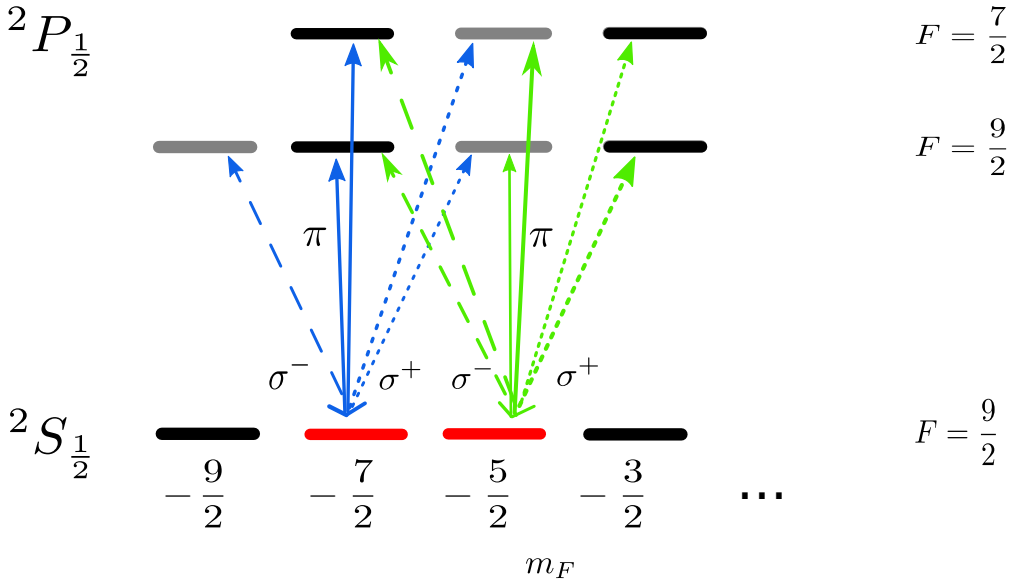

Figure 2.5: The energy level in the D1 transition of ^{40}K the two coupled levels are the $|\frac{9}{2}, -\frac{7}{2}\rangle$ and $|\frac{9}{2}, -\frac{5}{2}\rangle$ with blue and green arrows serve as the possible coupling upper levels. The long (short) dashed and solid are the $\sigma^-(\sigma^+)$ and π polarization respectfully.

By expending the Raman beams to be much larger from the atomic cloud, we can assume that the beams are essentially plane waves. Therefore each beam donates its wave-vector and polarization, which we can write as

$$\vec{k}_q = \frac{\omega_q}{c}\hat{e}_q^{\perp} \ , \ \mathbf{e}_q = \left(\sigma^+, \pi, \sigma^-\right) = \left(\frac{\hat{x} + i\hat{y}}{\sqrt{2}}, \hat{z}, \frac{\hat{x} - i\hat{y}}{\sqrt{2}}\right)$$

Here $\mathcal{L}, q$ represent the laser emitting the photon and the polarization of the photon. The second part is more elaborate and includes the atoms internal DOF and the effect of light on them. Looking at Equation 2.25 we can use the Wigner-Eckart theorem[26] to obtain the Matrix element that connects the initial energy state, and final using the quantum number at low-field transition [2]

$$\langle i|\,\mathbf{d}\,|f\rangle = \langle J, F, m_F|\,\mathbf{d}\,|J', F', m_F'\rangle = \mathcal{G}(J', F', m_F', J, F, m_F, I, q)\langle J\|d\|J'\rangle \qquad (2.31)$$

On the RHS, we have a function that only depended on the quantum number of the atom and the light polarization, multiplied by a matrix element of the dipole momentum

between fine structure levels. we can further write their dependency as follow

$$\langle J\|d\|J'\rangle = \sqrt{\frac{3\lambda^3\epsilon_0\hbar\Gamma}{8\pi^2}\frac{2J'+1}{2J+1}} = \sqrt{\frac{\epsilon_o c(2J'+1)}{4I_s(2J+1)}}\hbar\Gamma \quad , \quad I_s = \frac{2\pi^2\hbar c\Gamma}{3\lambda^3} \tag{2.32}$$

$$\begin{aligned}\mathcal{G} =& (-1)^{F'+F_{\min}+J_{\max}+I+m_F}\sqrt{(2J+1)(2F+1)(2F'+1)} \\ &\times \begin{Bmatrix} J & J' & 1 \\ F' & F & I \end{Bmatrix}_{6j} \begin{pmatrix} F & 1 & F' \\ m_F & q & -m'_F \end{pmatrix}_{3j}\end{aligned} \tag{2.33}$$

Here $\Gamma, \lambda, c, \epsilon_0$ are the natural line-width, wavelength, speed of light, and the vacuum dielectric constant. The $\{\}_{6j}, ()_{3j}$ are the Wigner 6j,3j symbols, and we call $\mathcal{G}$ the geometric factor which can be calculated for any transition between two sub-levels. In the following derivation we assumed $J = J' = 1/2$ which mean we are only working on the D1-line as seen in Figure 2.5. finally, we can combine all the factors together to get

$$\mathbf{\Omega}_{ij}^{\mathcal{L},q}(\mathbf{r}) = \frac{1}{\hbar}\langle i|\mathbf{d}\cdot\mathbf{E}_{\mathcal{L},q}(\mathbf{r})|f\rangle = \mathcal{G}_{ij}^{q}\Gamma\sqrt{\frac{I_{\mathcal{L},q}(\mathbf{r})}{8I_s}}e^{i\left(\omega_{\mathcal{L}}t-\vec{k}_{\mathcal{L}}\cdot\mathbf{r}+\phi\right)} \tag{2.34}$$

we use the relation $2\epsilon_0 c\left|E_{\mathcal{L},q}\right|^2 = I_{\mathcal{L},q}$ [17] this equation sums up all of the contributions from both the laser and the atom structure.we verified the geometric factor with [26] and we so no discrepancy between the numbers. We also wrote a full MATLAB code that takes the initial and final state and extracts the $\mathcal{G}$ factor for different transitions in the energy level structure of ^{40}K, which is found in Appendix A.

2.3.3 Cross coupling light-shift and Raman frequency

Because each laser can couple to both energy levels in our schematic we should take in to account this effect and sum over those optical transitions. Assuming zero two photons detuning $\delta = 0$ we add the stoke laser on the $|0\rangle$ and the pump on the $|1\rangle$ with the proper detuning from that level, so we write

$$\begin{aligned}\Lambda_{|0\rangle} &= \frac{1}{4}\left[\frac{\left|\mathbf{\Omega}_{0j}^{\mathcal{P}}(\mathbf{r})\right|^2}{\Delta_{0j}} + \frac{\left|\mathbf{\Omega}_{0j}^{\mathcal{S}}(\mathbf{r})\right|^2}{\Delta_{0j}-\Delta_E}\right] \\ \Lambda_{|1\rangle} &= \frac{1}{4}\left[\frac{\left|\mathbf{\Omega}_{1j}^{\mathcal{S}}(\mathbf{r})\right|^2}{\Delta_{1j}} + \frac{\left|\mathbf{\Omega}_{1j}^{\mathcal{P}}(\mathbf{r})\right|^2}{\Delta_{1j}+\Delta_E}\right]\end{aligned} \tag{2.35}$$

Now by using equation Equation 2.34 with summation over all possible transition we can calculate the multilevel light shift for each laser

$$\Lambda_{|i\rangle}^{\mathcal{L}} = \frac{\left|\mathbf{\Omega}_{ij}^{\mathcal{L}}(\mathbf{r})\right|^2}{4\Delta_{ij}^{\mathcal{L}}} = \frac{\Gamma^2}{32}\frac{I_{\mathcal{L}}}{I_s}\sum_{j,q}\frac{\mathcal{G}_{ij}^{q}}{\Delta_{ij}^{\mathcal{L}}} \tag{2.36}$$

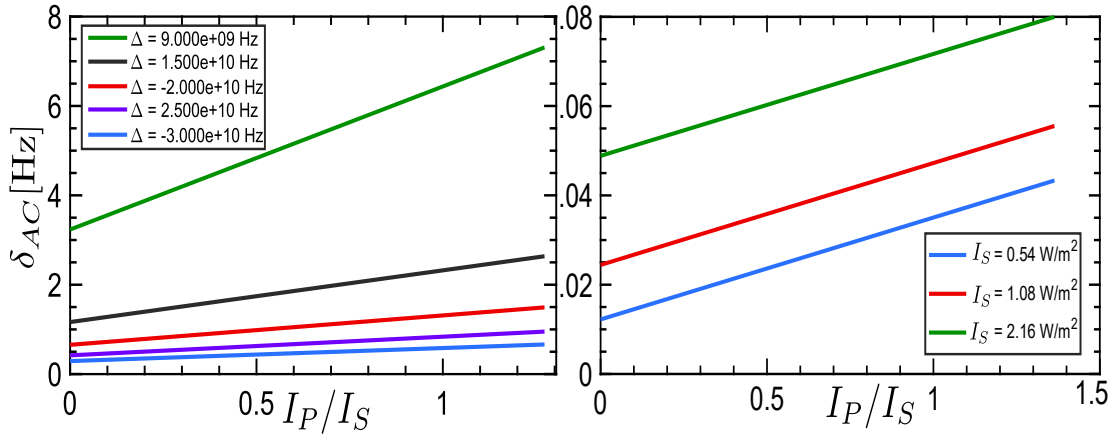

Figure 2.6: LHS: By changing the one-photon detuning, we can decrease the light shift effect as a function of the Raman laser power ratio. Even in low detuning (9GHz), the effect between our two energy levels is negligible. Of course, if we lower the detuning to be compared with the Rabi frequencies, the effectively empty third level assumption is no longer valid, so we must work with at least a few GHz detuning. RHS: setting the detuning to around 100GHz and changing the intensity of both laser has almost zero effect, meaning that will need extremely (1W) high laser intensities to observe any light shift effect in our Raman setup.

by implementing this equation while considering the cross coupling effect of each laser we can find the light shift with the use of Equation 2.27 applying it together we get

$$\delta_{AC} = \Lambda_{|1\rangle} - \Lambda_{|0\rangle} \tag{2.37}$$

We can plot the light shift as a function of the laser power ratio for our setup, which can be seen in Figure 2.6. From the right side of the graph, we observe that the light shift is in high detuning very low around 0.1Hz and the effect of the light intensity is significantly small. This means that we can increase our Raman beams to higher intensities without changing the transition rate. The fact that the calculation shows no dependency in the power of the beam allows us to transfer any amount of atoms we desire in any magnetic field with high confidence of its value, we will show that indeed there is no light shift effect in our working energy state with the Raman. The left image shows that going under certain detuning $\Delta < 9$GHz value, the light shift increases to several tens of Hz and even higher this give us an indication for our cutoff detuning that we should work above. We move on to look at the Raman Rabi frequency. if we look at Figure 2.5 we see that we have only two possible contributions to transfer atoms from the two Zeeman levels (in red) in the D1 manifold $|9/2, -5/2\rangle, |7/2, -5/2\rangle$. we can calculate their probability using equation Equation 2.26 and equation Equation 2.34 we get

$$\Omega_R = \frac{\Gamma^2\sqrt{I_P I_S}}{16 I_s} \sum_{q,j} \frac{\mathcal{G}_{1j}^{q_1}\mathcal{G}_{2j}^{q_2}}{\Delta_j} \tag{2.38}$$

From the light shift calculation, which adds up to be practically zero, and also because we work closely to the two photon resonance, we can write $\Omega_R \approx \tilde{\Omega}_R$. and Equation 2.38 give us the Generalized Raman Rabi frequency.If we plug some numbers $I_P = 2.75[\mathrm{W/m^2}], I_S = 2.16[\mathrm{W/m^2}]$ and detuning $\Delta_1 \approx \Delta_2 \approx \Delta = 10\mathrm{GHz}$ we get in our system $\tilde{\Omega}_R \approx 524.69\mathrm{Hz}$.

2.4 Probing the quasi-particle(QP) regime using Raman spectroscopy

Extracting the temperature T/T_F by fitting it to 1D power-law momentum distribution with the using Raman spectroscopy is only meaningful when the gas is in the weakly interacting regime. When strong interactions are at play, the symmetric distribution (as seen in Figure 2.2) is no longer dominant, and we observe an asymmetric line-shape as well. This Raman transition rate which we measure along with the BCS-BEC crossover, can give us an insight into how the spin-balanced homogeneous Fermi gas is transitioning as a function of the interaction near the Feshbach resonance. By locating the peak position we can calculate the mean-field energy E_{mf} and by fitting to a theoretical model, we might be able to extract the atoms pairs molecules binding energy E_b and quasi-particle weight Z.The fitting function development is construct by identify the two main elements in the Raman transition rate $\Gamma(\omega) = \Gamma_{\mathrm{coh}}(\omega) + \Gamma_{\mathrm{bg}}(\omega)$ here we refer to $\omega = (\omega_2 - \omega_1) - \Delta E/\hbar$ as the Raman detuning.The two terms are the first is the coherent part representing the symmetric peak in the line-shape. This part is proportional to the momentum distribution, which we computed for weak interaction. The second term correlated to the incoherent part of both the QP and molecule extending as a power-law tail line for high frequencies. Obtaining the expression for the Raman transition rate can be done by use of Fermi golden role

$$\Gamma_i(\mathbf{k},\omega) = 2\pi\Omega_R^2 \sum_j \mathcal{A}_{ij}(\mathbf{k},\omega) n_{\mathrm{FD}}(\mathbf{k},\omega) \tag{2.39}$$

$$\mathcal{A}_{ij}(\mathbf{k},\omega) = \frac{\left(e^{-E_j/k_BT} + e^{-E_i/k_BT}\right)}{\mathcal{Z}} \left|\langle\psi_{ij}(\mathbf{k})\rangle\right|^2 \delta\left(\hbar\omega + E_j(\mathbf{k}+\mathbf{q}) - E_i(\mathbf{k})\right) \tag{2.40}$$

we donate $n_{\mathrm{FD}}, N, \mathbf{q}$ as the Fermi-Dirac distribution the Grand canonical partition function $\mathcal{Z} = \sum_i e^{\bar{E}_i/k_BT}$ and the relative Raman momentum $\mathbf{q} = (\mathbf{k}_2 - \mathbf{k}_1)$.The $\psi_{ij}(\mathbf{k})$ are the based on the initial states, in our case we treat those terms as either molecular or QP states ;i.e. $|i\rangle = \{\psi_M(\mathbf{k}), \psi_{QP}(\mathbf{k})\}$.As a consequence of observation we can split the spectral function $\mathcal{A}_{ij}$ in two parts the coherent and the incoherent

$$\mathcal{A}_{ij}(\omega,\mathbf{k}) = Z\mathcal{A}_{ij}^{\mathrm{coh}}(\omega,\mathbf{k}) + (1-Z)\mathcal{A}_{ij}^{\mathrm{inc}}(\omega,\mathbf{k}) \tag{2.41}$$

here Z is the QP weight and after momentum integration and summation on all possible transition states $|j\rangle$ we can relate the $\Gamma_{\mathrm{cog,bg}} \propto \mathcal{A}^{\mathrm{cog,inc}}$.Procuring the right spectral

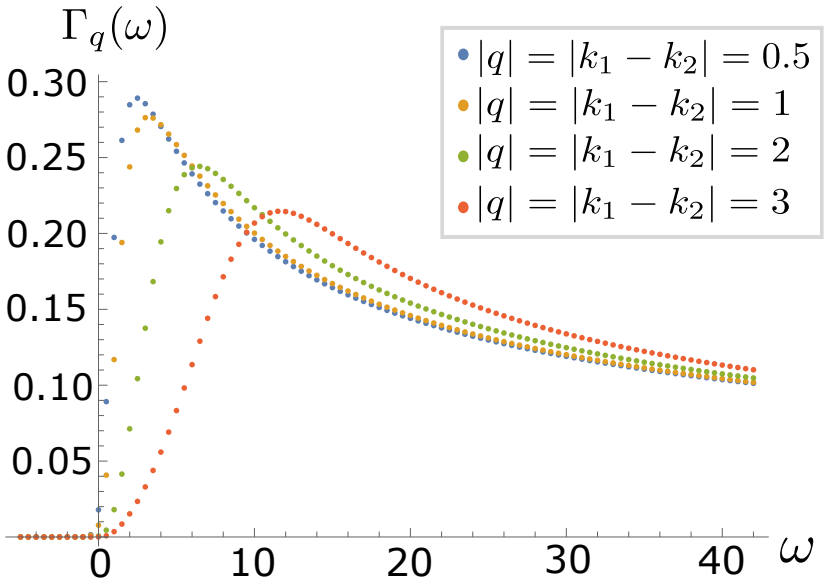

Figure 2.7: Caption

function is not always easy and may involve numerical solution for instance in evaluating the background transition rate term. To the end of this work, we will assume a spectral function of an imbalanced gas with a polaron and molecule excited initial states, and we will follow [34] fitting model only in the limit where we take the momentum distribution to be of a homogeneous gas instead of harmonic.However ,we can try to take into account the preformed pairs which in the BCS theory means that a sizable pseudo-gap (PG) emerges replacing the standard superfluid gap.Due to the presence of a pseudo-gap (PG) we can write a spectral function [8]

$$A(\mathbf{k},\omega) = \frac{1}{2}\left[1 - \frac{\mathbf{k}^2 - \mu}{\sqrt{(\mathbf{k}^2-\mu)^2 + \Delta_{pg}^2}}\right]\delta\left(\omega + \sqrt{(\mathbf{k}^2-\mu)^2 + \Delta_{PG}^2}\right) \tag{2.42}$$

Here δ, μ, Δ_{pg} are the Dirac Delta function the chemical potential and pseudo-gap parameter. In Equation 2.42 we assume low temperatures $\frac{k_B T}{\Delta_{PG}} \ll 1$ and together with the assumption of homogeneous gas distribution we get that the Raman transition rate in the PG theory

$$\Gamma_{\mathbf{q}}(\omega) = 2\pi\Omega_R^2 \int n_{\mathrm{FD}}(\mathbf{k}) A(\mathbf{k}-\mathbf{q},\omega) d^3\mathbf{k} \tag{2.43}$$

we plug in the spectral function the relative momentum of the two Raman beams $\mathbf{q} = \mathbf{k}_1 - \mathbf{k}_2$ and n_{FD} is the homogeneous Fermi-Dirac momentum distribution.Under Equation 2.43 we can get a momentum distribution for a spin-balanced homogeneous gas as seen in Figure 2.7.The model is not yet complete, so we could not extract physical parameters, and we will discuss what is needed to finish if we desire to revels new information regarding data in the strong interaction near the Feshbach resonance.

Chapter 3

Experimental setup

This chapter will describe how the experimental system was built and what had been implemented to achieve precise and stable measurements for long periods of time. First, we will describe the primary system (this part of the system constructed before my arrival to the lab and therefore only give a short review about it) and how we create the degenerate Fermi gas. Secondly, explain in detail the Raman laser setup, which will realize the $|F = \frac{9}{2}, m_F = -\frac{5}{2}\rangle \leftrightarrow |F = \frac{9}{2}, m_F = -\frac{7}{2}\rangle$ transition, and elaborate about the part in the setup enabling us to reach high and stable SNR using a Fabry Perot cavity. Finally, we will end with a brief explanation about the acoustic optical modulator(AOM), and its effects on detuning and controlling the Raman beams right before introducing them into the main setup.

3.1 The main system setup

As seen in Figure 3.1, the main system in the lab is composed of three different chambers, all under ultra-high vacuum and connected to each other. The atoms are taken from a heated Potassium dispenser around temperatures of 300^oC and then trapped and cooled by a 2D MOT (magneto-optical trap) beams in the first chamber. By using a push beam which is far detuned from the atom's resonance, we move them to a second chamber where a 3D dark SPOT MOT cools them even lower to a temperature of $T \approx 145\mu K$ with $N \approx 10^9$ on the D_2 line, from there a grey molasses D1 cooling is implemented and lower the temperature to $T \approx 15\mu K$ with the same NoA (number of atoms). In this part of the sequence, we cannot reduce the temperature without decreasing the NoA due to spontaneous emission caused by the collision inside the cloud. To continue reducing the temperature, we must magnetically trap and evaporate the atoms. To do so, we optically pump the atoms to hyperfine sublevels $|F = \frac{9}{2}, m_F = \frac{9}{2}, \frac{7}{2}\rangle$ and load them to Quadruple Ioffe configuration (QUIC) magnetic trap. The moment the atoms are magnetically trapped, we start the microwave evaporation processes. Next, we are left with $N \approx 20 \times 10^6$ that are loaded to a YAG laser optical dipole trap (λ =1064nm) with $T/T_F \approx 4.5$ transporting the cloud into a third

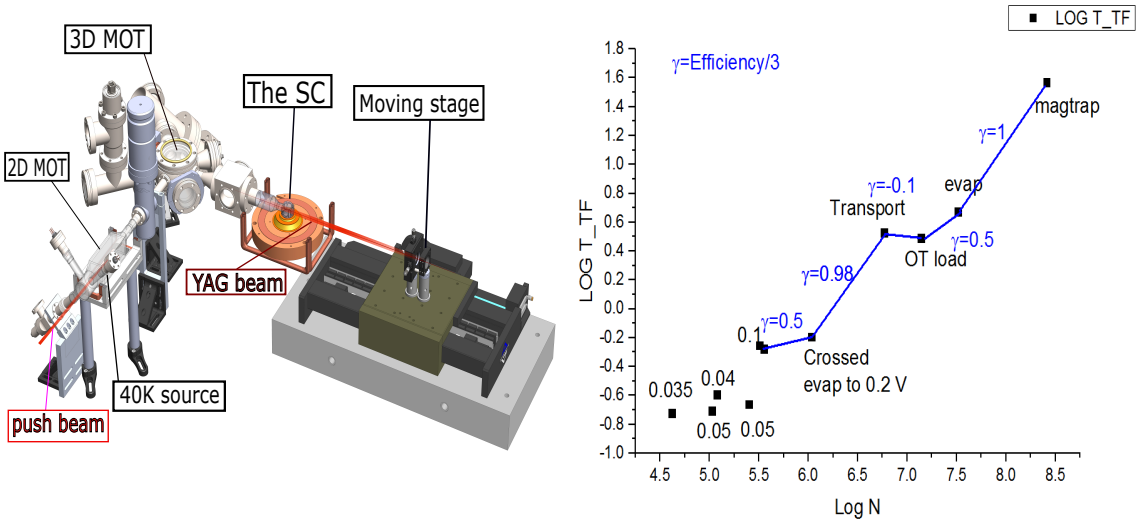

Figure 3.1: Left: the main system with all three chambers and the transport beams. The ^{40}K atoms evaporate from a dispenser and transport to the 2D MOT chamber. A push beam transfers them to a 3D MOT chamber where we cool them using a 3D dark SPOT MOT and Gray-molasses on the D1 transition. We use an optical pumping technique and at the same time lead them to a magnetic trap where we perform MW evaporation lowering the temperature to $T/T_F \approx 4.5$. The atoms are then loaded to an optical made by a YAG laser beam and transferred to the third chamber (SC) using a moving lens placed on an air-bearing stage where we cool them even further by decreasing the beam power reach temperature of $T/T_F \approx 0.15 - 0.2$.Right: following the definition for evaporation efficiency $\frac{\eta}{3} = \frac{\log(T/T_F)_i - \log(T/T_F)_f}{\log(N_f) - \log(N_i)}$ where i, f represent the initial and final stages between each transition. We can observe the efficiency of each step in our cooling system until the cloud reaches the SC.

chamber. This transition is done by moving a lens in which the YAG laser is passing throw, creating an optical tweezer with a waist of 40μm and power 2.4W. The lens motion is controlled by an air-bearing translation stage (Aerotech model ABL1500-200) that reduces the vibration and heating of the ensemble. The stage trajectory into the SC (third chamber) is implemented with an STA technique that ensures minimal NoA loss and optimizes the trap's cooling. This transportation method also shows in [18] was studied and published by another group member Gal Ness in 2019. Upon arrival in the SC, the cloud shape is broadened on its transport axis since the trapping potential is weaker compare to the perpendicular direction. To avoid atoms escaping from this direction, we bring a second crossbeam in 45° to the transport beam that strongly confined the atoms in this axial direction. Throughout the evaporation, we decrease the cross beam initial value from 2.5W to 1.8W and reducing the transport beam power to a few mW. During this process, we transfer the spins to a negative spin state by firing an rf pulse at a frequency of 4MHz and simultaneously ramping the magnetic field adiabatically from 11.4G to 14G in 13ms. Due to the enhancement of the Feshbach resonance in the negative spins states, we ameliorate the thermalization

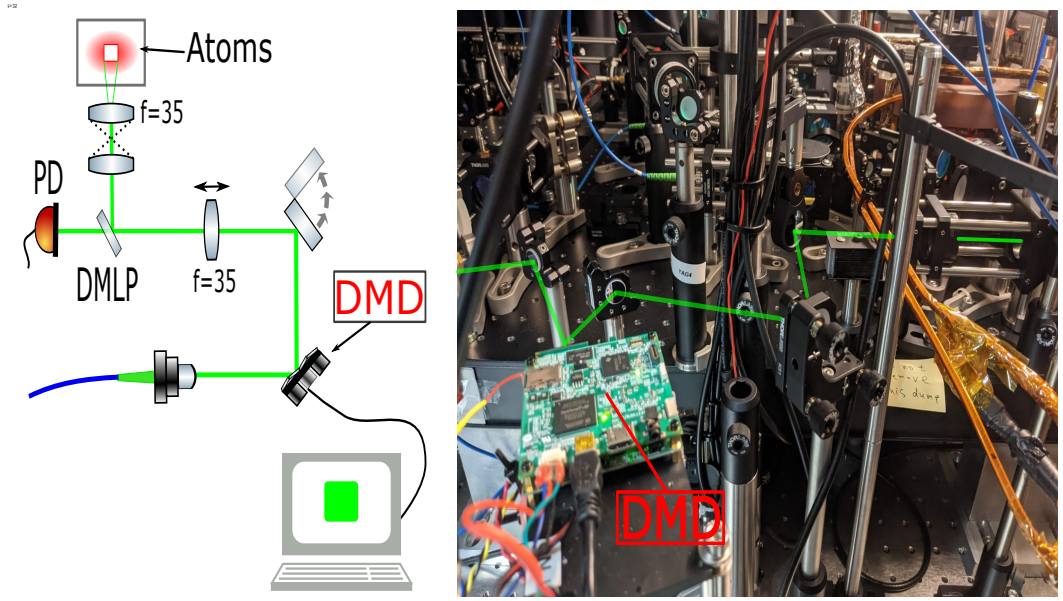

Figure 3.2: On the LHS, we can see a schematic image of the DMD system. The Verdi beam is lighting the device's surface, which is made of a diamond-shaped lattice of mirrors. A predetermined image is sent via computer to the DMD's motherboard, which is aligned based on the image. From there, the beam goes to a lens that focuses the light on the atoms. Using a PD just before the SC, we can control the laser power to a specific value. On RHS, the actual optical path of the beam before the SC.

rate of the ensemble. This sequence is known as adiabatic rapid passage (ARP), and following it, we ramp the magnetic field even higher to 185G, increasing the scattering length and shortening the evaporation time, leaving us with a 7:3 spin mixture ratio of $|F = \frac{9}{2}, m_F = -\frac{9}{2}\rangle$ and $|F = \frac{9}{2}, m_F = -\frac{7}{2}\rangle$. We blast the atoms with 30μs rf pulse rotating their spin until we reach a 50/50 balanced spin mixture which we measure with a Stern–Gerlach experiment. In the end, there are $N \approx 200 \times 10^3$ trapped atoms per spin state at a temperature of $T/T_F \approx 0.15 - 0.2$ we can evaporate, even more, losing atoms in the process and reaching clouds with $T/T_F < 0.1$. From this point on, we can experiment with the atoms inside a box potential where the gas is uniform distributed in space.

3.2 Box trap induce by digital mirror device(DMD) setup

After reaching the end of the evaporating cooling limit while the atoms are trap in the optical trap inside the SC, we slowly switch on a Verdi laser beam (532 nm). The beam is separated into two systems, one to create the "tube beam" from above and another to create the two caps beam. The two beams generated from one laser (laser model) resits on the optical table and transfer with two optical fiber to the main table where one fiber optical path leads to a splitting setup followed with a cylindrical lens that creates the two caps beam and is described in detail in [40] The other beam is directed to a second

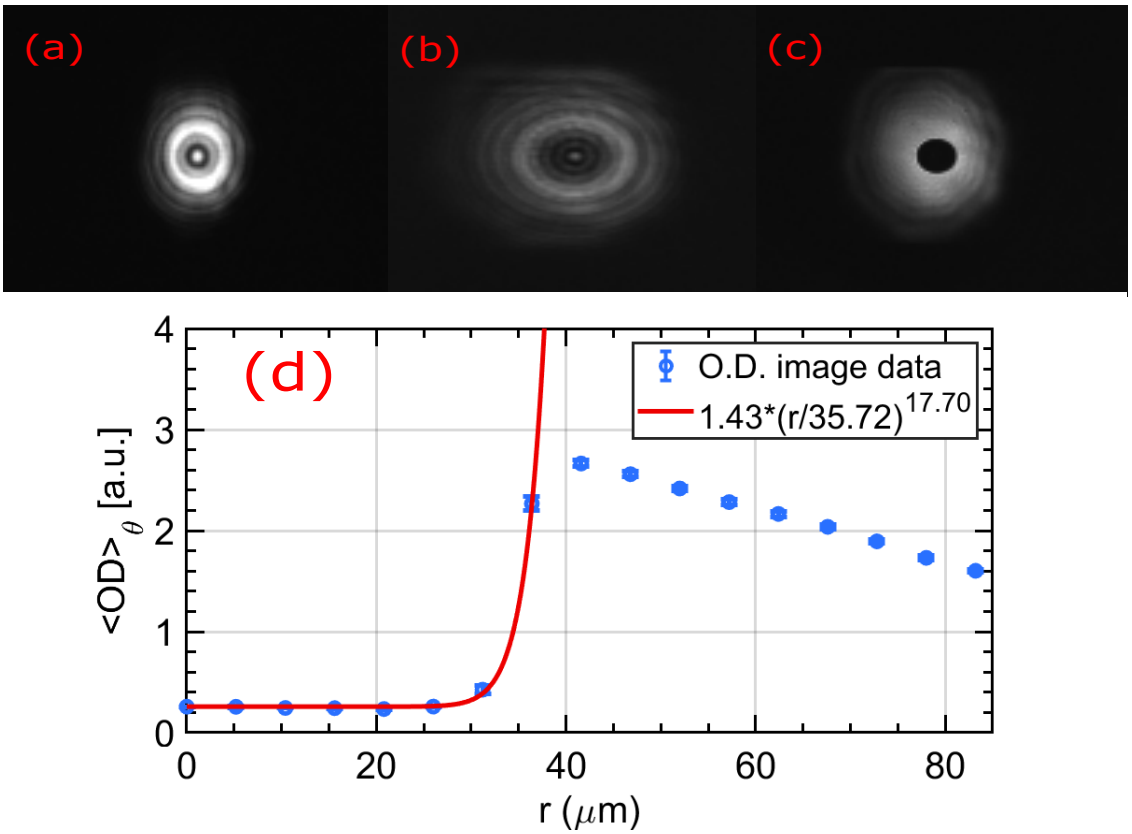

Figure 3.3: a tube shape images were taken outside the main system. (a) in-focus image (b) out-focus image (c) a focused image of the DMD tube imprint, using this image, we can find the focal distance to the main system and calculate the optical potential the atoms encounter. (d) by employing an azimuthal averaging in different radius in image (c), we can fit a power-law functional and extract the power and effective radius of the optical trap.

setup design to fabricate a 2D ring profile and effectively create 3D cylindrical-shaped walls from the top of the SC. Together those three-beam generate a dark region in which the atoms are transferred into and held inside. The circular confinement from above is done using a digital mirror device (DMD). This device imprint any configuration one desire using a grid of mirror of 608X648 in size. we can see this setup in Figure 3.2, we emit the beam on the DMD surface, from there, a series of mirror guide the light a lens mounted on the cage which can move back and forth so we can adjust the focal plane of the beam on the atoms To prevent diffraction and other optical effects, the DMD light must be focused precisely on the atoms. We built an external system similar to the system of the atoms and took images with different locations of the camera. this also helped us understand the optical potential that the cloud will experience. in Figure 3.3 we can see four images. The first three are camera pictures in a different location along with the optical path (a), and (b) are in and out of focus, and image (c) is exactly where the focus lies. Taking image (c), we can find the tube center and azimuth average around it, and we can then fit a power-law model to find the power and

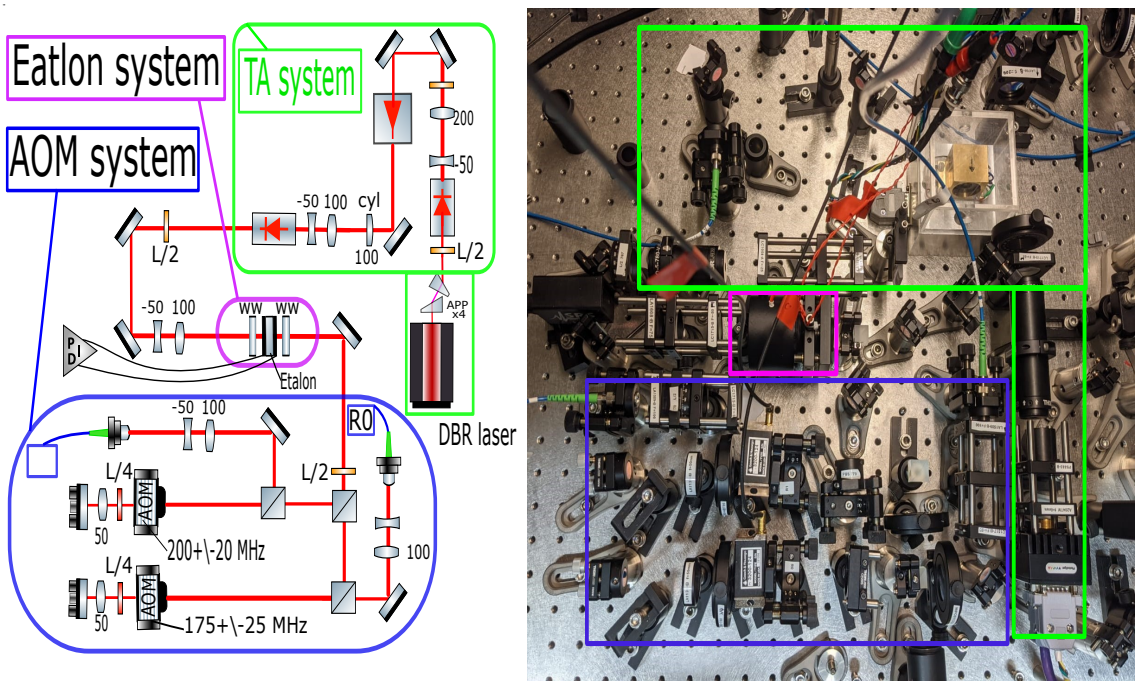

Figure 3.4: The complete Raman system, we can see on the left image each subsystem separately (green) the is the TA and laser system where the Raman beam is shot out and amplified, follow up with the steady temperature etalon system (magenta) that cleans undesired frequencies, the last part is the AOM system (blue) where we split the beam to two distinct rays and transfer them through AOM at which point each beam has a specific frequency and polarization going into the fibers and to main system. on the right side, an image of the actual system marked with the colors of each subsystem.

effective radius of the trap. Another advantage of the DMD is the ability to create any shape to imprint on the cloud and also change it during an experiment, this capability can help study dynamical aspects of Fermi gases, quantum gas expansions, and much more application some of them we started to explore and can be seen in **??** and also in appendix B

3.3 The Raman experiment setup

The Raman system is built out of 3 subsystems: the DBR laser and TA system, the temperature locked Etalon system, and finally, the AOM and power locking system. The following section will elaborate on each system separably, how it was built, and its uses. The main idea is to produce by a single DBR laser and an optical setup two beams (Raman) with different frequency and different polarization such that we get a specific transition in the atoms. The entire schema and actual setup is seen inFigure 3.4

3.3.1 Raman laser and TA system

The first part in the Raman is the 770nm distributed Bragg reflector (DBR) laser (Photodigm PH770). The laser is detuned from the D1 transition by 100GHz, and it is stable to around 50MHz.Its wavelength is determined by the temperature of the diode cavity and by the laser current ($\approx$ 150mA). Furthermore, those two parameters are set by an external controller (SRS LDC501) connected to the laser. After the laser, we use an Anamorphic Prism pair (APP) in order to get to transform an elliptical beam into a circular one. From there, the beam is transferred through an optical isolator (IOT-5-780-VLP) to shield from reflection back into the laser, following by a series of lenses and mirrors which guides the beam to the tapered amplifier (TA) system. The TA system as seen in Figure 3.5 is composed essentially of Saturated absorption (SA) (EYP-TPA-0765). This medium, through the use of electric current and seeding from a single frequency laser light, can create an "avalanche" effect of photons[7] thus amplifying the output beam. The other parts of this setup are the two aspherical lenses needed to insert the beam as accurately as possible and placed on a spinning mount to change their focal location. A brass mount holds all the previous parts, and between this mount and a large aluminum block which acts as a heat sink placed a thermal electric cooler (TEC). This electric device transfers heat from the brass mount to the heat sink, maintaining a stable temperature on the TA itself, which we constantly measure using a 10kΩ Thermistor (TH10K). This closed feedback loop setup allows us to change the temperature to any desire setpoint. This entire system is monitored with both current and temperature controllers (LDC240C and TED200C) on the right side of Figure 3.5.both the TEC and the Thermistor are connected to the temperature controller, which has a built-in PID circuit to fix the setpoint in a closed feedback loop. This system can increase the input laser power from 20 mW to 320mW with a current of 1A, and the current threshold is around 3A. In this current, the output power can reach around 1.6W. From there, the beam passes across a cylindrical lens, a telescope, and an isolator to collimate and prevent back reflections straight to the etalon.

3.3.2 Fabry perot cavity (etalon) and temperature locking circuit

In the Raman setup, we use an optical resonator name etalon(LightMachinery OP-7423), also called a Fabry Perot cavity. The etalon provides filtering for a broad frequency spectrum leaving the Raman beam with a narrow wavelength transmission. Thus, we can reach high SNR in the transfer of atoms between the energy levels. The idea behind the etalon design is to create an optical cavity as seen in Figure 3.6 in which lights bounce back and forth inside until eventually transmitted or reflected depending on the etalon parameters we can control how much light is passing and in which frequency. the Transmission function, which connects the initial and final intensity

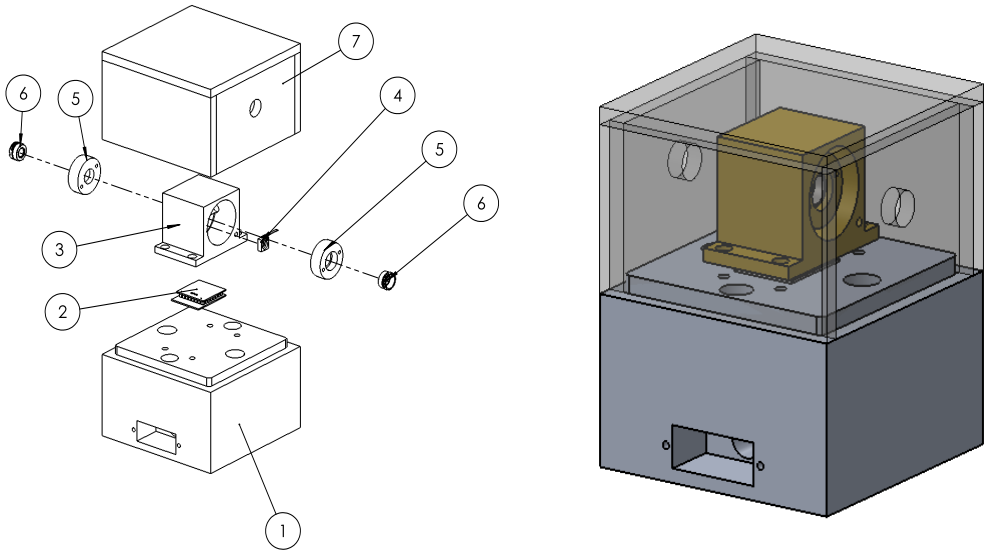

Figure 3.5: from left to right, left image the dissemble TA system (1) aluminum block (heat sink) holding all cables in this mount (2) thermal electric cooler (TEC) with the thermistor constructing the close temperature loop(3) brass mount (4) The TA with the SA and the compatible mount and connectors (5) two lens mounts (6) two aspherical lens (7) plastic shielding(8)10kΩ Thermistor.On the right image we see the full assembled TA system

$I_f = T_f I_i$ is written as

$$\frac{I_f}{I_i} = T_f = \left|\sum_{j=0}^{\infty} t_j\right|^2 = \left|t\sum_{j=0}^{\infty}(Re^{i\delta})^j\right|^2 = \frac{|t|^2}{|1-Re^{i\delta}|^2} = \frac{T}{(1+R^2-2R\cos\delta)} \tag{3.1}$$

here R, δ is the reflection coefficient of each surface assuming both side are identical ,and the phase difference which we can write as

$$\delta = \frac{2\pi}{\lambda} 2nl\cos\theta \tag{3.2}$$

This phase dependence on the wavelength λ the incidence angle of light inside the etalon θ the refracting index n and length of the etalon $l = l(T_e)$ which in our setup is a function of temperature. In the system, we set the etalon perpendicular to the beam, so $\theta = 0$ and the refracting index are constant. to get maximum transmission $T_f = 1$ we can manipulate a bit Equation 3.1 together with the equation of energy conservation $R + T = 1$ we get

$$\max(T_f) = 1 \Rightarrow \delta_m(\Delta T) = 2\pi m | m \in \mathbb{Z} \tag{3.3}$$

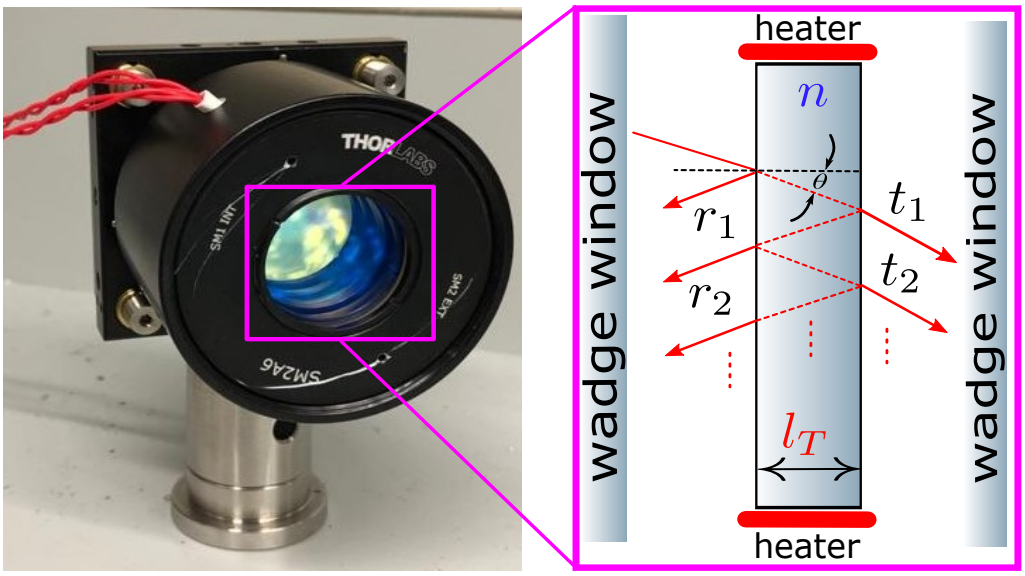

Figure 3.6: the 2 inch mount holding the etalon inside between two wedge windows (WW).two wires exiting the tube outer layer and are connected to stabilizing circuit which keeps the etalon temperature stable.on the right is an illustration of the inner tube, the etalon is in the middle of the WW and incoming rays are reflected and transmitted.the length of the etalon l_T is detriment by the temperature which is control by the heater surrounding the the inner tube.

if we assume that we can thermally stabilize the etalon at some temperature T_e we can write using A.1 (Appendix A)

$$\frac{\lambda_0^2}{2nl_T} = \Delta\lambda = \underbrace{\frac{\Delta\lambda}{\Delta T}}_{\alpha}\Delta T = \alpha\Delta T_{\text{DBR}} \tag{3.4}$$

Using the DBR laser Temperature controller, we are able to change the wavelength of the laser. With the use of Equation 3.4 we can find the wavelength(temperature) in which we will get maximum power after the etalon. The problem arises when we can not stabilize the etalon temperature, thus reducing the power transmitted after. We can see this in Figure 3.8 left image as seen a change of 0.5 Cel degrees can cause a loss of more than 50% in transmission. This effect is detrimental, and to overcome it, it had to build a stabilizing circuit using an Arduino Nano that will stabilize the etalon temperature. We first set the etalon inside a 1 inch isolated cylinder. We placed a thermal heater with a thermistor (HT 10K Thorlabs)on top of the cylinder, as seen on the left image (fig 3.9). Two wadge windows (WW) from each side of the tube were put to stop air from coming inside. This entire contraption was set in a 2 inch cylinder with thermal foam material between the inner tube and the outer one. Two cables were solder to the heater and extracted from a small hole in the outer tube, then connected to a PID circuit as seen in (fig 3.9). The 2 inch cylinder was placed

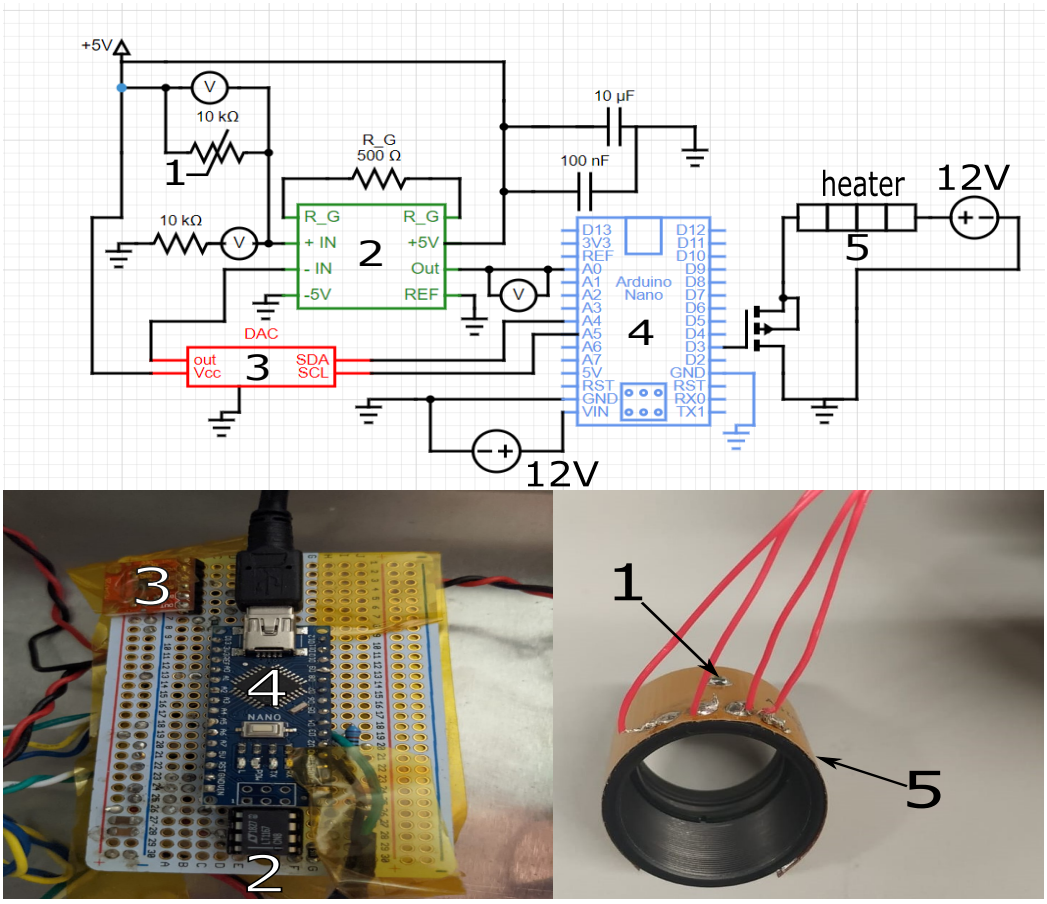

Figure 3.7: Top image: the etalon temperature stabilization setup. The Thermistor(1) is set close to the etalon, measuring the temperature, which is then converted to voltage (V_{ther}) and send to the GA (2). A set-point temperature is predetermined and upload to the Arduino (4) and converted as a digital voltage signal V_{sp} to the DAC, which convert it back to an analog signal to be detected from V_{ther} and amplify by the GA (2), and send to the Arduino(4). The Arduino using a PID code and PWM is changing the voltage on the heater (5) to match the desired voltage (V_{sp}).bottom left image: the breadboard with the GA, Arduino, and DAC sitting on it. bottom right image: The heater with the Thermistor grabbing on the etalon inner tube.

on an optical table with an adjustable mount to fix the incoming beam's angle. We build the PID circuit independently its full electric scheme is seen in top of Figure 3.7. The circuit is composed of 5 parts, and it enables us to correct the temperature change up to $\Delta T_e = 0.02$Cel. This precision is needed due to extreme sensitivity around the peak transmission after the etalon, as seen in (fig 3.8). We begin with a very stable($\pm 1\mu V$) 5 Volt reference supply to prevent outside noise on the thermistor. The thermistor voltage (V_{ther}) is entered into a Gain amplifier (LT1167 GA), this voltage is compared with a set-point voltage coming from the Arduino, which we set (V_{sp}).This voltage is converted by a digital to analog converter (MCP4725 I2C DAC) from the 1024bits in the Arduino. The two signals subtracted and multiply in the GA by the gain factor ($G = 100$) the signal is send to the Arduino $V_{\text{out}} = G(V_{ther} - V_{sp})$. On the

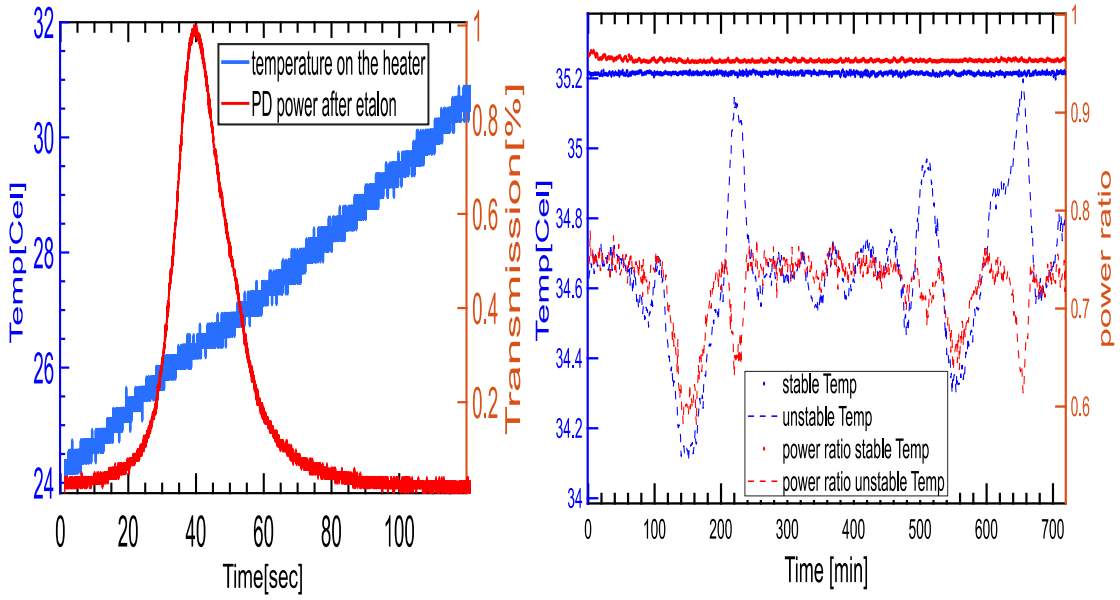

Figure 3.8: Left graph: By heating the etalon using the heater from $24 - 31$ Cel, we can see that the peak transmission is in a specific area of temperatures, but as we increase the temperature even higher its decreases again. In the temperature range where we have above 0.5 transmissions, the change is only 1 Cel. Right graph: The measured power after the etalon divided by the initial power together with the etalon's temperature as a function of time (12 hours) on a YY-axis graph. In-dash lines, the data is taken without using the stabilizing circuit, and in the dotted line is using the PID circuit. A constant factor moved the entire power ratio for the clarity of the graph. Note the stable dataset points of temperature and power ratio were moved by a constant shift for visibility.

Arduino, we implemented a PID code that brings $V_{\text{out}} \to V_{sp}$ by opening and closing the current passing in the heater using a PWM signal. The newly measured heater's voltage is measured by the thermistor and compared again with the resend V_{sp} from the DAC. Due to the effect of the Gain factor, this process changes the precision on the thermistor from $\Delta V = 10mV \to 0.1mV$, which we can see in Figure 3.8 on the left graph. Inside the Arduino code, We use the Steinhart equation, which connects the Resistance of an element to its temperature, together with the relation $R = \frac{R_0}{V_0/V_{ther}-1}$ we can measure the temperature on the heater as seen in the Figure 3.8 and the whole relation is found in (Appendix B), here R_0, V_0 are the room temperature Resistance and the power supply voltage respectfully.

3.3.3 Acoustic optical modulators (AOM) system

In order to generate a optical transition between two $|0\rangle, |1\rangle = |F, m_F\rangle, |F, m_F + 1\rangle$ energy level we need a photons with the frequency

$$E_{|1\rangle} - E_{|0\rangle} = \hbar\omega_{01} = h\Delta f$$

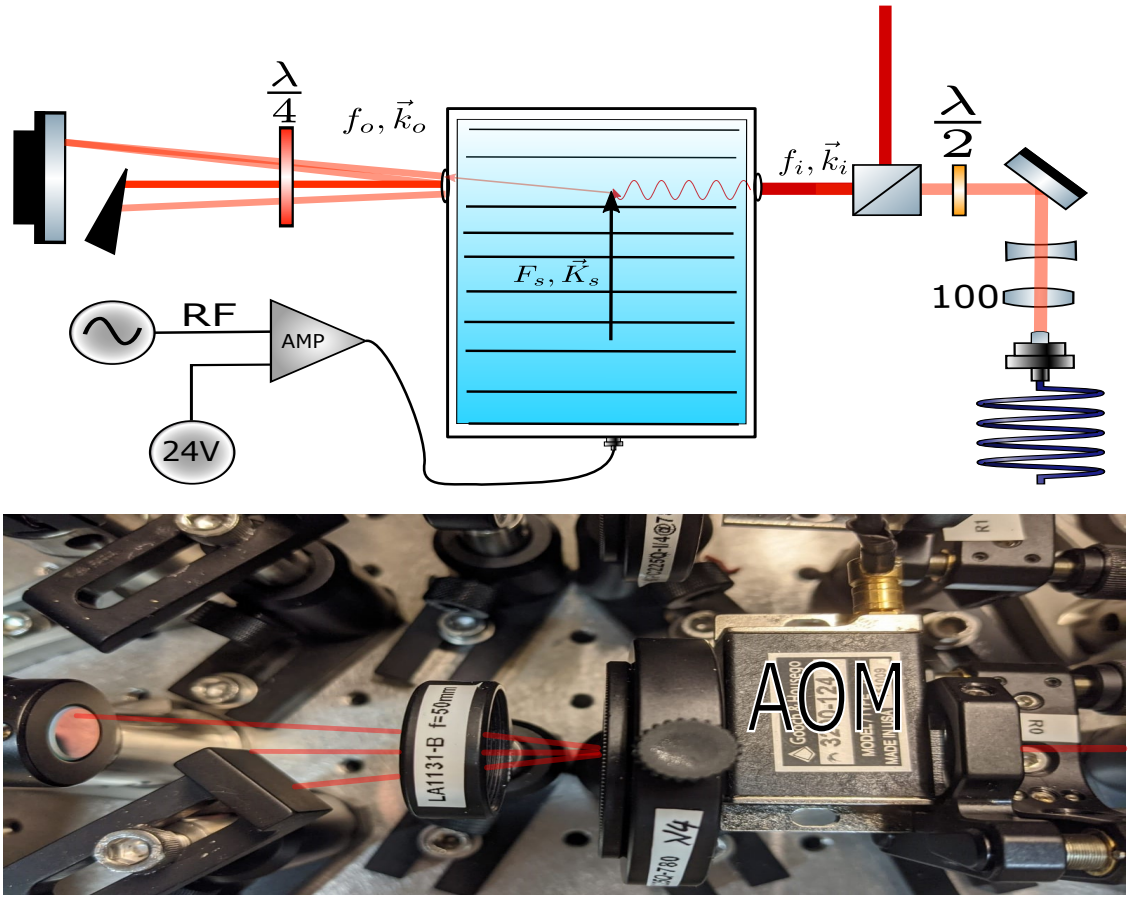

Figure 3.9: Top image: Close lookup of the AOM system.photon is inserted into the AOM with $f_i, \vec{k}_i$ frequency and wave-vector inside the crystal an RF phonon is propagating with $F_s, \vec{K}_s$ hits the photon and deflects it.the output beam is decomposed to number of modes $f_{o,m}, \vec{k}_{o,m} | m \in \mathbb{Z}$ with different powers and deflections angels.by blocking all beam except for the first mode $m = 1$ we get $f_{o,1} = f_i + 1 \cdot F_s$ this rays is reflected back by a mirror after passing twice in quarter plate which act as half plate $2 \cdot \frac{\lambda}{4} = \frac{\lambda}{2}$ and exiting from the AOM with $f_{o,1} = f_i + 2 \cdot F_s$ passing through BS, half plate and a telescope to control its final polarization and size entering the optical fiber.

But there is an issue that in order for two beams to have a difference in frequency of MHz, the change in wavelength needs to be

$$\frac{c}{\lambda^2} \Delta\lambda = \Delta f \tag{3.5}$$

here we took c, λ and Δf to be the speed of light ,the main wavelength and the frequency difference respectably,assuming of $\lambda = 770$nm which make $\frac{\lambda \Delta f}{c} \ll 1$.if we plug some number to Equation 3.5 we get that we need two photon with a difference in frequency of $\Delta f \approx 10^6$Hz which is almost impossible. To overcome this problem, we use an acoustic optical modulator(AOM). The idea is to shift the frequency of light with the frequency of the speed of sound inside the optical crystal. The operation of this device is seen in Figure 3.9 we can assume a beam entering the crystal of frequency $f_l = \frac{c}{\lambda}$

and a propagating phonon (sound particle) with frequency of $f_s = \frac{v_s}{\Lambda}$.so if the incoming photon frequency is leaving the AOM with a freq $f_i \rightarrow f_o = f_i + mf_s$ where m is the order of diffraction from the AOM if we take the same beam and splits it the pass in a different AOM and take the first order $m = 1$

$$\Delta f = f_0 - f_1 = f_i + mf_{s,0} - f_i + mf_{s,1} = f_{s,0} - f_{s,1} \tag{3.6}$$

because we control the frequencies that enter the crystal and the amplitude we can reach, depend on the AOM to any frequency and power in the crystal's limits.usually between $f_o = 0 - 500$MHz and power of up 2W. In ^{40}K, the two lowest groundstates energy difference is 45-50 MHz around the Feshbach resonance as seen in Figure 2.1. We can detune the number of atoms transfer between those two levels by changing the sent RF frequencies to the AOM's. In the setup itself as seen in Figure 3.4 in the blue section the light is transfer through an 50/50 NPBS which splits the beam to two identical beams with half the power of the original beam from there each beam goes into the AOM lower image in Figure 3.9 and forward to a double pass setup as seen in Figure 3.9.this insure that even if we change the insertion beam to the AOM the reflected beam will not deflects outward of the AOM. the beam are than reflected back by mirror again to the AOM after passing twice in quarter plate this acts as half plate maintaining the polarization of the light.when the two beam exiting the AOMs in the second time their frequency difference is $\delta f_{12} = (f_0+2f_1)-(f_0+2f_2) = 2(f_1-f_2)$ where f_0, f_1, f_2 are the DBR laser central frequency and the RF in each AOM 1 and 2, this means we can control the beams frequency difference by an generated RF signal send to each AOM.from that point we inject the beams to two optical fibres that opposed each other on the main table. Before the fibers, we implement a half plate and a small telescopic system to tune the light polarization and reshape its mode improving the power efficiency after the fiber.

Chapter 4

Experimental results

In this chapter, we present the result in several experiments. We start by looking at the spins oscillations dynamic generated by our periodically rf pulse, which leaves us with a uniform distribution inside the box. Then we show that there is no noticeable light shift due to the Raman beams in the system of ^{40}K, and we continue to elaborate on the Raman technique and how it is used to extract the atomic cloud temperature. We deduced that a pair condensation could be created in the box trap from the Raman data, and we observe it and measure its fraction. Towards the end, we present a new measurement of spectral line-shapes made with Raman spectroscopy of a homogeneous spin-balanced Fermi gas. This measurement is performed over the BCS-BEC crossover, meaning that the interaction strengths are being changed for each Raman measurement. From each line shape going from weak to strong interaction domain, We look at the peak position attributed to the mean-field energy and peak width, which both are model-independent quantities and can be extracted from the data without applying any fitting function.

4.1 Dynamics of spin oscillation in a box potential

Our experiments are preform with degenerate Fermi gas of ^{40}K, we start the experiment by cooling the gas to quantum degeneracy in two crossed optical dipole traps to improve loading efficiency to the box trap[41]. The process yields an anharmonic trap with $(w_r, w_z) \approx 2\pi \times (236, 27)$Hz as the radial and axial trapping frequencies. To load to the flat trap, we position the tube beam over the harmonically trapped gas and ramp it to 30mW already at the beginning of the evaporation in the cross trap. During the loading, a magnetic gradient field is ramp up to counteract gravity in the axial direction, and we continued ramping the Verdi caps and tube beams to 50mW and 150mW, respectively. The two traps overlap for around 50ms and then ramp down for 200ms the cross beam, leaving us with only the box trap. Typically the remaining atoms are around one third of the atoms in the harmonic trap. We end this sequence by force evaporation in the flat trap ramping down the power to 20mW and 50mW in the caps and tube beams,

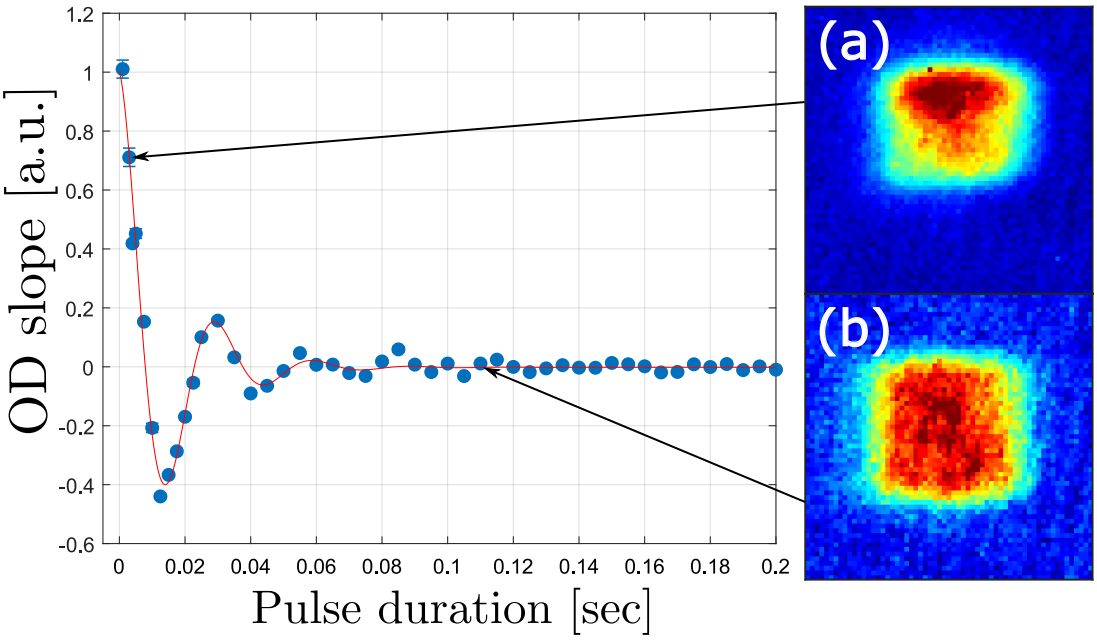

Figure 4.1: In the main plot, we see the density slope in the center of the flat-box trap as a function of the rf pulse duration. at $t = 0$, we switch the rf field on, and we see damped oscillation until after 110ms, the density relaxes to a uniform distribution.we fit the data to $f(t) = Ae^{-\frac{t}{\tau}} \cos(\omega t + \phi) + B$ and obtain the decay rate $\tau \approx 16ms$ and oscillation frequency of $\omega \approx 2\pi \times 33.6$Hz A, B, ϕ are the amplitude background signal and phase which have no relevance to our measurements. This measurement was done in a maNgnetic field $B \approx 203$G where the scattering length between the $|\downarrow\rangle$ and $|\uparrow\rangle$ is $a \approx 1152a_0$ (a_0 is the Bohr radius). The two left figures are *in situ* images taken from the side of the trap in 3ms and 110ms pulse duration for the top and bottom, respectively.

respectively, for 2s.The final typical conditions are $n \approx 60 \times 10^3$ in both spin state and $T/T_F \approx 0.16$. Even though the optical potential is flat, the total potential is not because the magnetic field, which supposes to eliminate gravity, has a differential effect on each spin due to their different magnetic moment $\mu_{|\uparrow\rangle} \neq \mu_{|\downarrow\rangle}$. So our ensemble is left non-uniform with only using a magnetic field. To ensure homogeneity of the gas, we had to implement a dynamical decoupling (DD) scheme. The idea discussed in chapter 2 relies on inducing an rf pulse that rapidly rotates the two spins. In our system, we start with a spin-polarized gas at state $|\downarrow\rangle$, initially, there is a 5.9% overcompensation when the magnetic field is set to $B_z = -\frac{2mg}{\mu_\downarrow + \mu_\uparrow}$ as shown in on the top right image of Figure 4.1 where most atoms are occupying predominately one part of the trap. So we set to find the time scale in which our gas is decoupled from gravity, and the densities start to equilibrate. The experiment begins with the gas prepared in only the $|\downarrow\rangle$ and being imaged from the side of the cylindrical box with every shot is made with a growing duration time rf pulse. To measure this process of spin relaxations from inhomogeneous to homogeneous gas, we used an *in situ* absorption imaging technique as seen on the left in Figure 4.1 which gave us the slope of the optical depth in the trap center. We

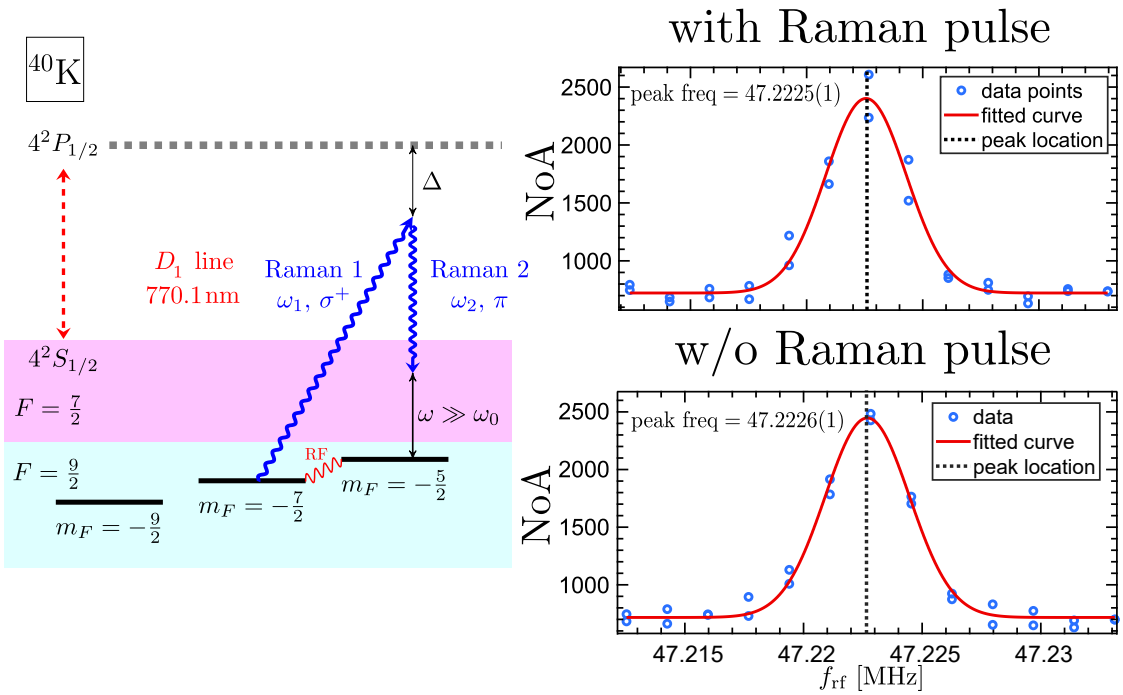

Figure 4.2: rf line shape measurements with and without applying a Raman pulse beams on the cloud.each points was measured twice to get a better accuracy the fitted curved is in compered to averaged of the two points.both peak position and FWHM are almost identical even due one is projected with 1ms Raman pulse.

plotted the normalized slope as a function of the pulse duration, setting its frequency to $\Omega \approx 2\pi \times 15.7$kHz shown in the main graph on Figure 4.1. We can see that after some damped oscillations around 110ms, the gas reaches a steady-state around zero slope value and become uniformly distributed. Therefore all of the following experiments are conducted with a pulse duration of 200ms to ensure homogeneity of cloud.

4.2 Detuning and light shift

To verify that the Raman light does not cause a shift in the magnetic field we set to conduct an experiment in which we prepare a balanced mixture of two states $\{|\uparrow\rangle, |\downarrow\rangle\} = \left\{|\frac{9}{2}, -\frac{7}{2}\rangle, |\frac{9}{2}, -\frac{9}{2}\rangle\right\}$ in the harmonic trap. Afterward, we transfer them to our box trap, where we use the DD pulse for 200ms generating a uniform cloud. Right after the end of the pulse, we apply simultaneously an off resonances Raman pulse and an on resonance rf pulse, which is detuned to the unoccupied state $|3\rangle$. We Raman is a Blackman shape pulse with a duration of $1000\mu s$ while the rf is a square pulse with $700\mu s$ and is programmed to overlap (their temporal pulse center is equal) entirely. The rest of the sequence is utterly identical to the last section high sensitive measurement using the $|4\rangle$ state.We repeated this experiment by changing the on resonance rf frequency each time and repeating the same point twice for more accurate measurement. We then used a Gaussian fit with the center and FWHM as free parameters calibrating the transition

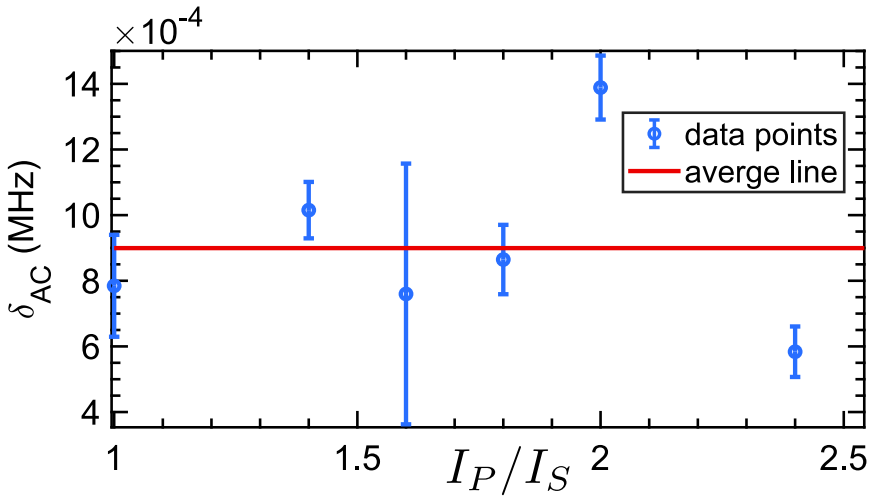

Figure 4.3: light shift vs Raman beams power ratio:we increased the power at one laser only and measured the peak location as seen in Figure 4.2 at different power.each point is repeated three times from which we see the error bars.the red line is the averaged of all 6 points and its about $\langle\delta_{\mathrm{AC}}\rangle \approx 900$Hz which is around our precision for this measurement.

frequency and energy level linewidth as seen in Figure 4.2. The magnetic field was set to a non-interacting regime $B \approx 209$G, and the Raman one-photon and two-photon detuning were $\Delta \approx -103$GHz and $\delta \approx -500$kHz,respectfully.we can see that there is no visible difference between the two measurements, and we even tried various changes such as replacing the Blackman with a square pulse and even lowering the detuning to a few tens of GHz with no significant shift in the peak position. Lastly, we measured this almost zero effect by the light shift, in which the intensities ratio was raised. The stock laser has been fixed to 1.1mW, and by increasing the pump laser intensity up to 2.64mW, we increased the power ratio. we observe no meaningful change as seen in Figure 4.3. Each data point was extracted from a Gaussian fit center and was averaged three times. We can see in Figure 4.3, the peak to peak light shift as a function of the intensities ratio is no more than 0.9kHz is in our error resolution, meaning we can not observe any change due to the Raman laser power.

4.3 Non interacting homogeneous Fermi gas

After verifying our gas is uniform and that the Raman does not shift the magnetic field, we set out to find our degenerate Fermi gas temperature. Usually, we can let the gas ballistically expend inside the SC for some ToF until the cloud is sufficiently distributed, and we can image it to fit with an FD distribution and extract the temperature from the fit [40]. When trying to let an initially large ensemble expand in a flat box potential, we see that the times needed to measure the temperature accurately are not always feasible.

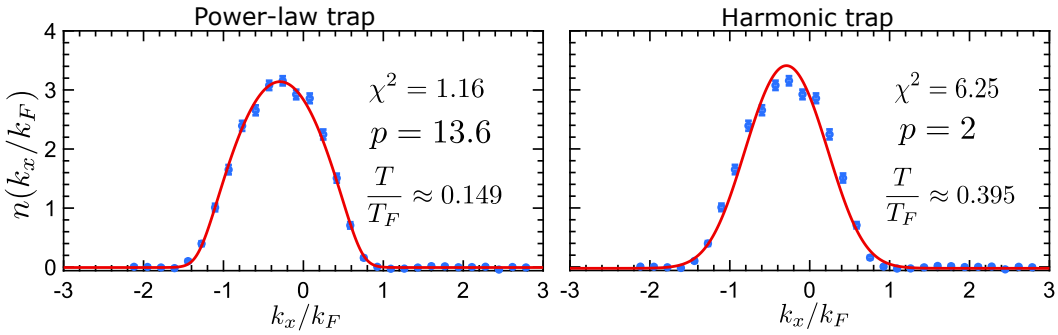

Figure 4.4: Raman momentum distribution in non-interacting Fermi gas. Left:The 1D momentum distribution fit Equation 2.18 for the non-interacting Raman data where each points was repeated three times and the fit was weighted using those points std.The power is set to $p = 13.6$ (see text) and the $\chi^2 = 1.16$.Right:Taking $p = 2$ and plugging it as the fitting function give $\chi^2 = 6.25$ far from representing the data correctly and also the temperature $\frac{T}{T_F} \approx 0.395$ is high compere to the usual conditions in box trap.

To overcome this issue, we implemented a Raman sequence in the non-interacting regime $B_{exp} \approx 208G$. The Raman process is done while the ensemble is still in the trap, and therefore, we do not depend on the size of the cloud and how long it will expend outwards. The measurement is made in the following way: we start the experiment with a spin balanced gas of the two spins states $|\uparrow\rangle, |\downarrow\rangle$. The atoms are transferred to the box trap by ramping up the Verdi caps and tube beams to 50mW and 150mW, respectively, while ramping down the cross and transfer beams to zero. During that time, we cross the Feshbach resonance using a double ARP sequence to minimize loss due to Strong interaction in the resonance field ($B_0 = 202.14G$).The field is then adiabatically ramped to a non-interacting regime $B_{\text{non-int}} \approx 209G$, and we further cool the cloud by lowering the Verdi beams intensities, thus evaporating the most energetic atoms out of the box trap. Before turning the Raman beams on, we apply a 200msec RF mixing pulse to rotate the spins in the box rapidly until we see that the spins relax, as seen in Figure 4.1. We then apply a 1ms two Raman beams, which are programmed to follow along with a Blackman pulse shape[3]. This pulse window helps distinguish the prominent peak from the side-band preventing spectral leakage, ensuring the atoms experience only the Raman frequency.The two Raman pulses transfer a small fraction of atoms from the $|\uparrow\rangle$ to an unoccupied state $|3\rangle = |F = \frac{9}{2}, m_F = -\frac{5}{2}\rangle$ allowing us to count the NoA compassionately. For one to observe only a few atoms, a fourth state is required. We use a 1ms MW pulse sweeping the frequency across 0.2MHz inducing ARP and transferring atoms to a fourth state $|F = \frac{7}{2}, m_F = -\frac{3}{2}\rangle$, this state is in a different hyper state, so those atoms have an opposite sign in the magnetic moment hence we can trap them while repelling all other atomic states we have in the optical trap. We are then left with only atoms in the fourth state to detected them. We turn on the MOT beams and start collecting photons emissions from the atomic cloud, letting us convert them to the number of atoms that have transitioned. The full scheme of described

sensitive detection is depicted in [41].The Raman transition connects atoms with initial momentum and energy stats $\hbar\vec{k}, E_i(\vec{k})$ to a final one with $\hbar(\vec{k}+\vec{k}_{\text{rel}}), E_f(\vec{k}+\vec{k}_{\text{rel}})$ where $\vec{k}_{\text{rel}} = \vec{k}_1 - \vec{k}_2$ is the relative wave-vector of the Raman lights.By assuming conservation of momentum and energy, before and after we use the Raman field, we can relate the two-photons detuning with the gas momentum along the Raman beams axis [43]

$$\Delta\omega = \frac{\hbar}{m}\left(\vec{k}+\vec{k}_{\text{rel}}\right)\cdot\vec{k}_{\text{rel}} \tag{4.1}$$

Here m is the atomic mass, and $\Delta\omega = \omega_1 - \omega_2 - \frac{\Delta E}{\hbar}$ is the Raman two-photon detuning where $\omega_1, \omega_2, \Delta E$ are the Raman beams frequencies and the two states energy difference. By changing the difference frequency between the two Raman beams with the AOM's, we can change the gas momentum projection along the Raman beams axis. Now because $\Delta\omega \ll \omega_1, \omega_2$ we can write $|k|_{\text{rel}} = \frac{4\pi}{\lambda_R}\sin\left(\frac{\theta}{2}\right)$ here λ_R, θ are the averaged wavelength of the two Raman beams and the angle between them (which is π in our setup), giving us a linear relation from Equation 4.1 and assuming we use Raman pulses such that their duration follows a linear response which means $\Omega_R t_R \ll 2\pi$.From Equation 2.38 we know that the pulses duration time scale needs to be around $t_R \approx 1\mu s$.We see in Figure 4.4 the results of the experiment conducted at a magnetic field of $B_{\text{exp}} \approx 209.1$ together with two fitting models.The first is a power-law model, which we developed at chapter 2 with $p = 13.6$, an effective power-law of the tube and the two caps beams for the box trap. The second one is the limit of the harmonic trap where we take $p = 2$. We can clearly see that the power-law model fits the data much better and from the χ^2 parameters that agree more with it. Using this model, we can extract the temperature as a free parameter, which in the case of the $p = 13.6$ gives us $\frac{T}{T_F} \approx 14.9$ indicating that we are at the regime of the Superfluidity phase transition $\frac{T_c}{T_F} \approx 0.167$ and it is possible to observe pair condensation forming in the gas ,So we set verify this assumption.[42]

4.4 Pair condensation in a homogeneous box

Certain materials undergo a phase transition into a superfluid under some critical temperature where their viscosity parameter vanishes, and they behave as a frictionless liquid. A well-known example is the Bose-Einstein condensation, where almost all of the ensemble's bosons occupy the groundstate as the temperature drops below a critical point and becomes superfluid. The same phenomenon was observed [16, 37, 49] in pairs of fermions projected to bosonic molecules and condense as we change the interaction of the Fermi gas going to unitarity from the BCS side. Experiments have shown [31, 25, 20] that the temperature in which this condensation fraction (CF) appears is around $\frac{T_c}{T_F} \approx 0.167$ and as we saw in the previous section, our gas temperature is around this area. To probe this many-body physical parameter, we set an experiment [42] based on changing the magnetic field near the Feshbach resonance. We begin our experiment with a balanced mixture of two spin $\{|\uparrow\rangle, |\downarrow\rangle\}$. First, our magnetic

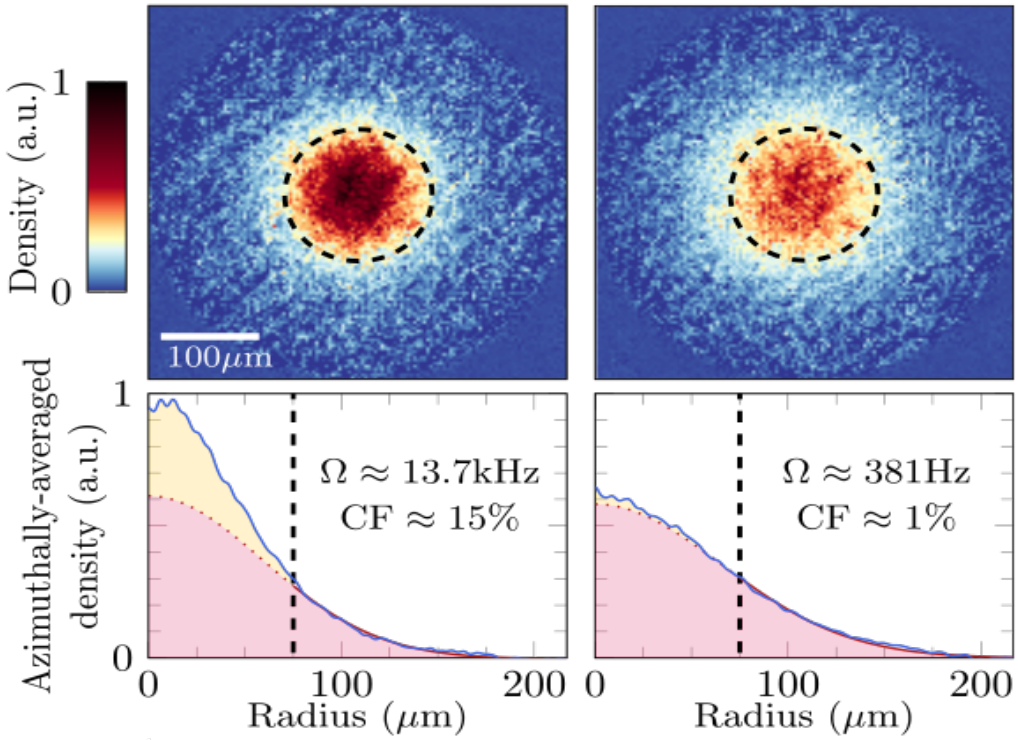

Figure 4.5: Condensation fraction in uniform Fermi gas. Upper panels: absorption images of the atomic cloud averaged over ten experimental repetitions. Right: when the rf pulse heats the gas going above $T > T_c$, and we see(lower panel) a homogeneous thermal distribution which we can fit a Gaussian (red line). From the signal above the fitted Gaussian, we extracted the condensation population, which is 1% in this image. Left: when the gas is under $T < T_C$, a peak rises above the normal distribution, and the yellow shading is more significant, giving us CF of 15%. Note that the radius (black dashed line) should be large enough to leave only the thermal distribution wings for the fitting.

field set to $B_{\mathrm{BCS}} = 203.5G$ in the BCS side where we have weakly interacting cooper pairs with opposite momentum, during which the DD sequence is employed to reach a uniform distribution. We then adiabatically ramp the magnetic field for $10ms$ to unitarity $B_0 = 202.14$, where they pair up and condense. Since the magnetic field is varying, we had to programmed the rf pulse frequency to track the resonance transition. To this end, the trap is turned off with the rf field, and we rapidly ramp ($40\mu s$) the magnetic field to the BEC side of the Feshbach $B_{\mathrm{BEC}} = 199.8G$ where we wait for about $20ms$ before go back rapidly to unitarity and image the cloud from above. In the last procedure, the weak bound pairs are projected onto a tight bound molecule with a background of particles that did not condense and escape the trap's center. Looking from upward positions on the ensemble, we see a bimodal distribution with a peripheral region represented with a thermal distribution and a condensation fraction of fermionic pairs appearing as a pronounced central peak as seen in Figure 4.5. In our experiments, we studied several CF parameters, such as the rf pulse frequency, which

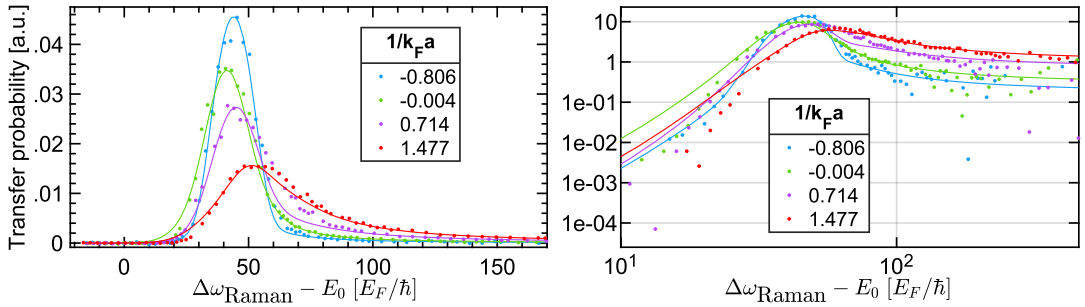

Figure 4.6: Raman line-shapes near the Feshbach resonance. Left:The transfer probability distribution for the Raman transition as function of the frequencies difference on linear plot.Each color represent different interaction going from weak $(k_F a)^{-1} = -0.806$ in light-blue to strong $(k_F a)^{-1} = 1.477$ in red.Right:plotting the same data on a log-log scale and multiplying the date by a $\Delta\omega^{\frac{3}{2}}$ factor to show that the developing tail in the high frequencies regime is flatten,indicting that the scaling goes like a power-law $\Delta\omega^{-\frac{3}{2}}$.

affects the CF percentage, and we can see two cases in Figure 4.5. Using the CF, we established that the rf pulse does not heat the atomic cloud proving the theoretical statement we presented in subsection 2.2.3. The CF measurement emphasizes Raman spectroscopy's reliability in providing an accurate prediction of our Fermi gas state.

4.5 Strongly interacting spin-balanced uniform Fermi gas

We moved on to use the Raman as a tool to investigate the strong interaction arises around the Feshbach resonance. In the non-interacting experiment we were able to find the temperature of our cloud but near the resonance the line-shape is not symmetric and it is unknown how one can extract the temperature.Nevertheless we can still find and measure other interesting observable emerging along the BEC-BCS crossover with the use of Raman spectroscopy.By changing the scattering length $a(B)$ we can change the strength of interaction between the two spin stats,so if we measure the momentum distribution of our balanced gas in different magnetic field creating a Raman spectra for each point and from this line shape see the effect of interaction on the thermodynamics of the atomic gas.We repeat our previous experiment only now the magnetic field is ramp towered the Feshbach resonance $B \in [201.9, 202.3]G$ we can map it to the dimensionless parameter $(k_F a)^{-1} \in [-0.91, 1.47]$ using the NoA in each experiment.First during the experiment we take 5 measurements of magnetic calibration with an rf pulse the same way as been described at section 4.2 just without the Raman being applied,and we also take 5 measurement of ToF to find the NoA for that experiment.With the magnetic field and NoA we can calculate the scattering length and Fermi momentum [40] and find the interaction strength for each magnetic field around the Feshbach resonance.We see in Figure 4.6 four line-shape at different interaction,each data-set point was repeated four times and weighted to use in the fitting

model.we see on the left image the linear plot and on the right image the log-log scale plot.There are some deviation of the fit at higher frequencies and also at lower ones,this deviation from the data might be because the fitting model is made for the imbalanced case and based on observation of a polaron-molecule transition [34] and not for the spin-balanced case,so there is no guarantee that the fit will sits well with the data.As seen in **??** there is some resemble to our data in Figure 4.6,and a fitting sequence is being prepped as this words are written down and hopefully in the future will be in use.

Chapter 5

Summary and outlook

5.1 Summery

In this work we have implemented and executed a Raman spectroscopy measurement probing the weak and strong interaction existing in a quantum gas of fermions. We conducted those experiments in a uniform distributed ensemble, which we show in both theoretical and experimental aspects that it is feasible to produce in our setup. We began by introducing our fermionic particle of ^{40}K and describe its energy structure. By laying out the physics behind trapping and cooling those atoms, we could go into details and present a more general model of captured Fermi gas in a power-law potential and derive some analytical equations for several thermodynamics quantities. An important assumption we based our trapping model on is that there are no external potentials other than the trap itself. For that to occur, we present a dynamical decoupling scheme that utilizes both an rf field to periodically drive the two spin components of the gas and a magnetic field to counteract gravity. Ultimately at the end of the processes, we reached a homogeneous gas where the potential is flattened. The next step was to acquaint Raman transition and its effects on cold atoms that we can observe. We then move on to our own specific case of transition between the two groundstats in the Zeeman splitting of the $^2S_{\frac{1}{2}}$ hyperfine level $|F = \frac{9}{2}, m_F - \frac{7}{2}\rangle \rightarrow |F = \frac{9}{2}, m_F = -\frac{5}{2}\rangle$.Summing on all possible different transfer states gives us the generalized Raman Rabi frequency and light shift, which we show negligible compared to the latter. Next, we present the main system and the new segments added to conduct the Raman spectroscopy experiments. We provide a brief explanation of how the system is built and produce degenerate Fermi gas, and then we show how we implement a box potential using a DMD and two caps of green laser beams. We proceed to the Raman system and detail how it was re-engineered to yield high power and spectrally narrow beams. The first part was to amplify the laser light with a tapered amplifier, and the beams then pass through an optical filter. This optical element is known as an etalon, and in order to maximize transmission efficiency, we had to stabilize its temperature. The Raman system's final part is the AOM setup, where we split the single beam in two and use each AOM to

control the beam intensity and frequency before it enters the optical fibers and arrives at the atomic cloud. Lastly, we presented the experimental results we found in our measurements, and we start by reporting a successful dynamical decoupling using an rf pulse which induces spin relaxation into a homogeneous gas. By taking absorption images from the box's side over different pulse duration, we can find out how long it will take the density slope to reach a zero point around the trap center. We continued with verifying the Raman light shift does not affect the atoms by observing any such shift even with increasing laser power. By employing the Raman beams on the non-interacting gas, we managed to produce a momentum distribution along the light direction, which complied with the power-law theory, gave an excellent agreement with our data, and enabled us to extract the temperature of the gas.

5.2 Outlook

The immediate step forward is to establish a proper fitting sequence to the strongly interacting spectral line shape under the assumption of a spin-balanced gas in a homogeneous trap. There are several candidates to accomplish this task. For the first one, we will choose the pseudo-gap approach, which assumes a spectral function that depends on the pseudo-gap replacing the standard superfluid gap in the BCS theory [8] and we introduced and presented it in section 2.4. The new model can help us extract novel physical properties such as the Z QP residual[34], which regrades molecules and QP formation as we cross from the cooper-pair in the weakly interacting BCS regime onto the tightly bound pair projection in the BEC domain. Another interesting new investigation direction we can adopt would be implementing a Raman beam that varieties over the cloud spatially. We can imprint with the two lights an azimuthal phase generating a Gauss-Legree first mode GL_{01} and fundamental transverse mode TEM_{00} in the second beam[10]. Furthermore, if one can take the 3D gas and adiabatically contract it into 2D Fermi gas [21], he can afterward use the Raman technique to generate an azimuthal phase over the cloud, which topologically protects the ensemble in theory.This particles collective behavior is referred in the literature as a 2D magnetic skyrmion[14, 6, 1].some of the several implementations [38, 46] This QP attributed to a property of having in its center one spin state and on the outer region the opposite spin, which means we can treat it as small magnets having some topological charge. Taking a step further, we can use a spatial light modulator (SLM) as a tool to form higher modes of light and projecting them onto the atomic ensemble. The SLM device has already shown abilities in creating a multi-array of optical tweezers [30, 11] in and capture atoms in those tweezers [32], Now together with the Raman process, we might be able to create higher-order QP and explore their interaction and lifetime.